



Contents lists available at ScienceDirect

Materials Science & Engineering A

journal homepage: www.elsevier.com/locate/msea

Microstructure and residual stress evolution during cyclic elastoplastic deformation of AISI316L fabricated via laser powder bed fusion

Marco Beltrami^{a,*}, Marco Pelegatti^a, Michele Magnan^a, Alex Lanzutti^a, Maxim Avdeev^{b,d}, Vladimir Luzin^{b,e}, Matteo Leoni^c, Francesco De Bona^a, Enrico Salvati^{a,**}

^a Polytechnic Department of Engineering and Architecture (DPIA), University of Udine, via delle Scienze 206, 33100, Udine, Italy

^b Australian Centre for Neutron Scattering – ANSTO, New Illawarra Rd, Lucas Heights, NSW, 2234, Sydney, Australia

^c Research and Analytical Services Department, Saudi Aramco, PO BOX 62, Dhahran, 31311, Saudi Arabia

^d School of Chemistry, The University of Sydney, Sydney, 2006, Australia

^e School of Engineering, The University of Newcastle, Callaghan, NSW, 2308, Australia

ARTICLE INFO

Keywords:

AISI 316L stainless steel
Metal additive manufacturing
Residual stress
Microstructure
Low cycle fatigue
Dislocations density

ABSTRACT

In metal additive manufacturing (MAM), microstructural properties such as texture, residual stresses, and dislocation density have emerged as key factors ruling the resulting mechanical performances. In this study, cylindrical AISI 316L specimens, fabricated with laser powder bed fusion (LPBF), were tested under cyclic elastoplastic (EP) deformation using a constant strain amplitude to highlight the evolution of residual stresses (RS), dislocation density and texture with increasing number of EP cycles, N , across the hardening-softening (H-S) transition stage, in the attempt to find correlations between relevant microstructural parameters and macroscopic properties. The structural and microstructural analysis is carried out through whole powder pattern modeling (WPPM) of neutron diffraction (ND) data and Electron Back-Scattering Diffraction (EBSD) analysis. The H-S transition is found to occur within 7–9 cycles, with RS fading out already after 5 cycles. Across the H-S transition, the trend of the maximum tensile stress correlates closely with the trend of WPPM-calculated total dislocation density, suggesting a major role of dislocations' characteristics in the evolution of macroscopic mechanical properties. EBSD analysis reveals the rearrangement of geometrically necessary dislocations (GND) into cellular structures, and moderate grain refinement, which are deemed to be responsible for the quick fading of RS in the very early stage of EP loading. ND-based texture analysis reveals a (220) preferential orientation retained throughout the EP tests but with orientation density functions (ODFs) changing non-monotonically with N , suggesting preliminary partial randomization of grains around the deformation axis followed by the recovery of crystallographic anisotropy and more localized ODFs.

1. Introduction

Additive manufacturing (AM) technologies consist of the fabrication of constructs in a layer-by-layer fashion, in which a feedstock material is locally melted and welded according to computer-aided design models [1,2]. The unmatched design flexibility of MAM technologies offers the potential to create SS components with novel three-dimensional design opportunities for lightweight components. Therefore, AM technologies have the potential to answer the growing need for resource-efficient, customized, high-value, low-volume production of engineering components [3]. In the metalworking industry, Selective Laser Melting (SLM),

also known as Laser Powder Bed Fusion (LPBF) is the most widely adopted among the various metal additive manufacturing (MAM) technologies being developed [4–6], accounting for over half of all MAM solutions [7]. Current research endeavours aiming at optimizing the MAM fabrication processes concentrate on correlating process parameters (e.g., the scanning strategy, hatch spacing, energy density) to the resulting microstructural properties [8,9] or to relevant engineering properties, such as fatigue resistance [10–12], or chemical stability in corrosive environments [13], while the main classes of feedstock materials consist of nickel alloys and steels. Among these, austenitic Stainless Steels (SS) play a vital role in various engineering applications

* Corresponding author.

** Corresponding author.

E-mail addresses: marco.beltrami@uniud.it (M. Beltrami), enrico.salvati@uniud.it (E. Salvati).

<https://doi.org/10.1016/j.msea.2024.146416>

Received 19 December 2023; Received in revised form 21 March 2024; Accepted 24 March 2024

Available online 26 March 2024

0921-5093/© 2024 The Authors. Published by Elsevier B.V. This is an open access article under the CC BY-NC-ND license (<http://creativecommons.org/licenses/by-nc-nd/4.0/>).

due to their outstanding combination of corrosion resistance, oxidation resistance, strength, and ductility [13–15]. Compared to conventionally fabricated (e.g., wrought or cast) counterparts, MAM SS components express improved yield strength [16], ductility-to-strength balance [17, 18], and physical/chemical stability. This is primarily attributed to the peculiar solidification microstructure consisting of columnar grains and melt pool structures whose size, morphology, and orientation depend on factors such as laser energy density and build direction [19,20]. Due to rapid cooling during the LPBF, these columnar grains are further subdivided into Cr/Mo-rich segregation dendrites [21,22] and dislocation structures [23], which originate from the fast, directional solidification imposed by the thermal gradients established within the material during the fabrication process. This microstructure yields a unique combination of strength and ductility, thanks to the possibility of further refining the microstructure by appropriate choice of process conditions [24–26]. It is accepted that the absence of such distinctive solidification microstructure in wrought or cast austenitic SS [27] is responsible for the lower yield strength, poorer strength/ductility ratio, and wear resistance of conventional SS versus LPBF SS [28,29]. Also, a secondary hardening stage due to a strain-induced martensitic transformation, and detrimental for the late ductility of the cycled material [30] is typically observed in conventional SS [30–32], albeit this has also been occasionally reported to occur for LPBF SS [33].

The improvement of fatigue performance of LPBF SS is of paramount importance aiming at a widespread adoption of MAM steels in engineering applications. In this context, most of the research efforts have focussed on the materials response under high-cycle fatigue (HCF) regime [34–37], while a comparable effort has not been adequately seen regarding the low-cycle fatigue (LCF) regime. As recently underscored by Pelegatti et al. [38], along with the limited number of studies, further impediment is caused by challenges in comparison due to diverse feedstock materials [39], process conditions [40,41], native defects density, location, and morphology [42–44], post-treatments [45], test temperatures [46–48] and employed equipment [49]. However, improving the knowledge of LCF behaviour of SS is of paramount importance. In fact, when used as a structural material for engine walls, pressurized water reactors, and nuclear power plants [50,51], structural SS endure significant thermal stresses and cyclic EP deformations during startups, shutdowns, or operating transients, therefore operating under an LCF frame [51,52]. It is well known that the cyclic EP response of LPBF austenitic steels such as the 316L typically comprises a hardening (H) phase and a subsequent softening (S) phase. This bimodal response arises from the evolution of the solidification microstructure of LPBF steels under EP deformation [20,21]. As discussed by Pham et al. [53], at the onset of cyclic EP loading, dislocations density increases at grain boundaries to maintain coherence between misaligned neighbouring grains, and within the grain due to the mechanically induced dislocation generation, both impeding the plastic flow [54]. With increasing EP cycles, intergranular strain inconsistencies are mitigated through the activation of secondary slip mechanisms, promoting dislocation interactions. These interactions result in the rearrangement of dislocations into organized cellular domains with high dislocation density on the walls and lower density in the interior [55–57], as well as the partial annihilation of dislocations at high and low angle grain boundaries (HAGBs and LAGBs) [58,59].

Despite this knowledge, due to the complexity of MAM processes and lack of enough experimental evidence, the widespread adoption of MAM technologies in the SS manufacturing industry, especially for large-scale structural parts, is currently limited. Key challenges, highlighted in recent reviews [60,61], include high initial costs, the absence of standardized design guidelines, low productivity, and expensive scaling-up. Another critical issue is the unpredictable introduction of material inhomogeneities at the microstructural level, such as porosities [62–66], surface roughness [67,68], and residual stresses (RS) [69–72] in printed parts. The presence of these inhomogeneities, especially the simultaneous presence of tensile RS and porosities [73,74], can deeply impair

the functional performance of the AM materials by promoting crack initiation and its propagation [75,76]. As a result, as shown for instance by Mower and Long [77] and by Gonzalez-Nino [78], MAM steels often express poorer fatigue strength than wrought counterparts. The compensation of such flaws demands thermal or mechanical post-treatments [79–81] at the expense of the overall process efficiency [61,82], and is not always technologically applicable [36]. A powerful and more cost-efficient route to improve the performance and reliability of MAM SS lies in gaining a deeper understanding on which materials properties need to be accurately optimized during the printing process. While the understanding of the specific role of cell and dislocation structures [46,47,83–86], defects [42–44,64], crystallographic orientation [87–89] and residual stress [90–92] in determining the fatigue properties of SS is consolidated, some previous works highlighted the need of considering the mutual interaction among multiple microstructural factors and their impact on the mechanical response [93–95]. Nonetheless, despite its potential to gain deeper design capabilities, to the best of our knowledge, this comprehensive approach is still poorly adopted.

Therefore, aiming to offer a comprehensive approach to the topic, this study seeks to investigate the impact of cyclic EP deformation on the microstructure and residual stress of LPBF SS, with a specific focus on the changes occurring across the hardening-softening (H–S) transition. The analysis involves the utilization of neutron diffraction (ND) and Electron Backscattered Diffraction (EBSD) techniques, described in the **Materials and Methods** chapter. As reported in the **Results** chapter, ND patterns were used to determine the RS within the bulk of the mechanically loaded section, following a defined number of loading cycles, while a line profile analysis enabled the evaluation of the total density of dislocations. Additionally, ND was employed for texture analysis within the bulk of the loaded samples section. EBSD was employed to establish a direct link between the extent of EP deformation and the corresponding microstructural information, including phase indexing, crystallographic orientation, grain size, and shape, and the distribution of GNDs. Proceeding through the **Discussion** chapter efforts are directed towards relating macroscopic observables such as cyclic hardening-softening and residual stress evolution with the corresponding evolution of dislocations density and organization as well as crystallographic texture. Finally, in the **Conclusions** chapter the main results are summarized and their use for future developments is indicated.

2. Materials and Methods

2.1. Materials and manufacturing

The determination of the chemical composition of feedstock powders and printed specimens, as well as the specifications of the manufacturing processes have been previously reported [38]. The feedstock material consisted of spherical particles of AISI 316L SS with an average diameter of 28.9 μm . Four cylindrical rods of 180 mm in height and 23 mm in diameter were produced using a Concept Laser M2 (General Electric) additive machine equipped with an IR laser of wavelength 1070 nm. The chemical composition of the rods, reported in **Table 1**, was measured by glow discharge optical emission spectroscopy (GDOES). Details of the manufacturing parameters are reported in **Table 2**.

The rods were built on the building platform with the long axis parallel to the build direction. An “island” scanning strategy was employed, dividing each layer into small neighbouring 5×5 mm squares in a chessboard pattern. The islands were then formed by melting consecutive bidirectional tracks. Adjacent islands were scanned along mutually perpendicular directions. To promote structural homogeneity, successive layers were printed by a 90° rotation and 1 mm shift along both in-plane orthogonal directions of each island. After removal from the base plate, each rod was stress-relieved at 550 $^\circ\text{C}$ for 6 h and eventually machined to a final cylindrical dog-bone geometry according to ASTM E606. The surface roughness parameters were obtained using a

Table 1

Composition in wt% of AISI 316L SS powders and LPBF rods.

Element	C	Cr	Ni	Mo	Mn	Si	P	S	O	Fe
Powder	0.02	17.70	12.70	2.35	1.14	0.65	<0.045	0.004	–	Bal.
LPBF rods	0.02	17.6	12.80	2.30	1.10	0.65	<0.004	0.004	0.0245	Bal.

Table 2

Parameters used for the LPBF process.

LASER POWER (W)	SCAN SPEED (MM/S)	SPOT SIZE (MM)	HATCH SPACING (MM)	LAYER THICKNESS (MM)	ATMOSPHERE GAS	RESIDUAL OXYGEN (AT. %)
180	600	120	105	25	Ar	0.2

Dektak-150 stylus profilometer (Veeco), in agreement with BS EN ISO 21920 2022. The arithmetic average roughness along the gauge length R_a , gave a mean value of $0.52 \pm 0.03 \mu\text{m}$, whereas the root mean-square roughness R_q , was $0.61 \pm 0.03 \mu\text{m}$.

2.2. Cyclic elastoplastic tests

The cyclic elastoplastic (EP) tests were performed on a servo-hydraulic MTS 810 machine equipped with a 100 kN load cell and an axial extensometer (model MTS 634) with a gauge length of 25 mm (measure range is $+5 \text{ mm}/-2.5 \text{ mm}$). We conducted strain-controlled tests using a triangular waveform with an amplitude of 0.4% and zero mean strain, maintaining a strain rate of $4 \cdot 10^{-3} \text{ s}^{-1}$ by appropriately adjusting the frequency of the waveform for each test. The moderate (0.4%) strain amplitude is deliberately chosen to permit plastic deformation without imposing excessively large variations into the material so that the specific effect of cumulative cycling could be better observed. As reported in the Supplementary Information file, section S1, the number of cycles to failure for this kind of specimen at the given strain amplitude and rate was previously determined to be about 15000 cycles [38], before which a two-stage mechanical response consisting of a hardening and a softening regime was observed. As discussed by Pham et al. [54], the initial condition of the steel and its early response to cyclic EP deformations are of major importance in the determination of the whole material's behaviour until failure. On this basis, three cyclic loading routines were set using the parameters listed in Table 3, with force and strain recorded at each cycle, aiming to observe the microstructural response during the hardening stage (5 cycles, sample code-name S-5), and in two moments within the early softening stage (200 and 3000 cycles, sample codenames S-200 and S-3000 respectively). Also, an as-built specimen (S-AB) was characterized to inform the initial conditions.

2.3. Neutron diffraction

Neutron diffraction (ND) has found widespread adoption in the investigation of microstructural properties of MAM materials [19, 96–102]. Its success is primarily due to its high grain statistics and penetration depth, which contrast with the limited sampled volume and surface or sub-surface constraints of either laboratory and X-ray diffraction [99], enabling accurate quantification of macroscale RS [103] and texture [104] also in the increasingly important *in-situ* [95, 105] and *operando* [96,99] analysis modes.

In this study, ND measurements were carried out at the Australian Neutron Scattering and Technology Organisation (ANSTO). For residual

Table 3

Parameters used for the elastoplastic deformation tests.

MAX. STRAIN (%)	STRAIN RATE (S^{-1})	CYCLES (N)	LOAD RATIO, R_e
0.4	0.004	0, 5, 200, 3000	-1

stress and texture analysis, the KOWARI strain diffractometer [106] was employed, selecting neutron beams with a constant wavelength of 0.153 and 0.142 nm respectively from the Si (400) monochromator at take-off angles of 90 and 62°. For RS analysis, as-built (S-AB) and fatigued (S-5, S-200, and S-3000) specimens were vertically mounted and fixed on the sample stage exposing the central cylindrical portion to the incoming neutron beam. The spatial distribution of the hoop (H), radial (R), and axial (A) RS components (see Fig. 1) for the four specimens were calculated from the shift in the 2θ position of the (311) reflection. This choice is optimal for analysing RS in mechanically deformed FCC materials [107]: as recently reported by Choo et al. [108], more intergranular strain is allowed to accumulate along the (311) reflections upon deformation, while the RS along $[h00]$ and $[hhh]$ directions is easily flattened due to slip mechanisms. For each direction, a linear scanning mesh of 13 points across the diameter was analysed by recording the (311) reflection, using a step-size of 0.75 mm and a voxel size of $1 \times 1 \times 1 \text{ mm}^3$. The sampled volumes were centred on the specimen's central axis to ensure the symmetry of the measurement locations. For strain calculations, a constant d_0 assumption was made in such a way as to ensure the stress boundary condition (for the radial component) and force balance conditions (for the hoop and axial components). For the calculation of residual stresses, the required isotropic Diffraction Elastic Constants (DEC) for a cubic system, S_1 , and S_2 , are necessary to account for mechanical anisotropy. The values of such constants were $S_1 = -\nu/E = -1.4501$ and $S_2 = (1+\nu)/E = 6.4504$, computed using stainless steel's macroscopic Young's modulus, $E = 200 \text{ GPa}$ and Poisson's ratio, $\nu = 0.29$. Each stress component σ_i^{hkl} , where

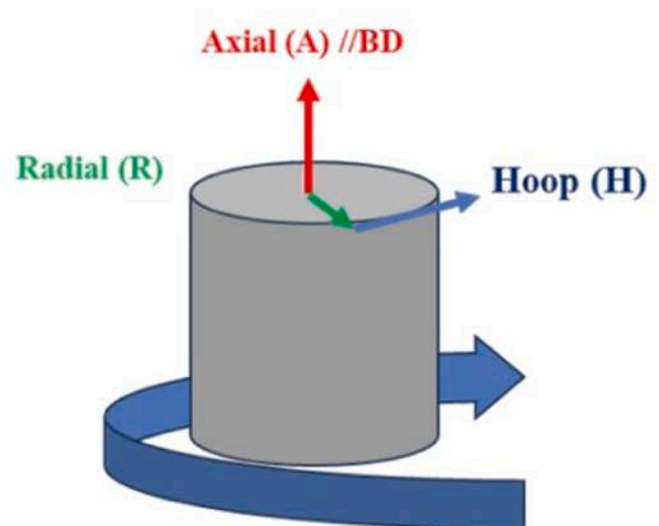


Fig. 1. Residual stress components analysed via neutron diffraction concerning the gauge volume in the dog-bone specimens. The bottom arrow represents the specimen rotation along the longitudinal axis during the acquisition of diffraction signal.

{hkl} are the Miller indexes of the chosen reflection (here {311}), was computed for each point of the 1D mesh using the following form of Hooke's law [100,109]:

$$\sigma_i^{hkl} = \frac{1}{S_2} \cdot \left[\epsilon_i^{hkl} - \left(\frac{S_1}{S_2 + 3S_1} \right) \cdot (\epsilon_i^{hkl} + \epsilon_j^{hkl} + \epsilon_m^{hkl}) \right] \quad \text{Equation 1}$$

where i, j , and m are interchangeable subscripts referring to the H, R, and A components of the RS. To plot RS components as a radial function, an axial symmetry approximation was imposed by averaging RS value pairs at a symmetrical distance from the central axis.

For texture analysis, cylinders 10 mm in diameter and 15 mm in height were cut from the center of the fatigued region of the dog-bone specimens. The measurements were run with a ca. $3^\circ \times 3^\circ$ mesh in φ - ψ space, where φ and ψ are goniometer angles that are transformed into the spherical angles in the sample coordinate system, over the intervals $[0, 90]$ in φ and $[0, 360]$ in ψ . Three detector positions $2\theta = 43^\circ, 67^\circ$ and 82° corresponding to the (111), (200), (220), and (311) reflections were selected to measure the complete pole figures (PF) of the given reflections. A total $\varnothing 10 \times H 15$ [mm] volume was analysed to ensure adequate grain statistics and a short acquisition time of 3 s. The analysis of texture data was performed using MTEX [110–112] (version 5.9). Orientation distribution functions (ODF) specify the volume fraction of crystallites having an orientation in the infinitesimal orientation volume $dg = \sin(\Phi) d\varphi_1 d\varphi_2 / 8\pi^2$, where g is a compact expression for the orientation defined in terms of the three Bunge's angles ($\varphi_1, \Phi, \varphi_2$) [113]. Here, ODFs were calculated on normalized PFs using a half-width of 5° . Ultimately, the texture index J_{ODF} , defined by Mainprice et al. [114], as a measure of the degree of preferred orientation:

$$J_{ODF} = \int |f(g)|^2 dg \quad \text{Equation 2}$$

Where $f(g)$ is the reconstructed ODF from the PF set. For a completely random specimen, $J_{ODF} = 1$ for all reflections, where a $J_{ODF} > 1$ or $J_{ODF} < 1$ for a subset of reflections indicate a stronger or weaker preferred orientation, respectively.

Line profile analysis was performed on ND data acquired using the ECHIDNA high-resolution powder diffractometer [115]. Full diffractograms in the range of 4° – 163° were collected with the same counting statistics using a neutron wavelength of 0.1622 nm at a take-off angle of 140° , with an angular step size of 0.05° . During data collection, the samples were rotated around the axis. The Whole Powder Pattern Modelling (WPPM) technique, implemented in the PM2K software developed by Leoni [116–118] was employed for the data analysis. As reported in the Supplementary Information file, section S2, to account for the instrumental contributions to the line profile, a LaB_6 (SRM 660a) NIST standard was also analysed in the same experimental condition as for the four SS specimens. Contrary to traditional LPA, where some arbitrary "microstrain" and "average size" values are usually computed, the WPPM is based on physical models for the line-broadening sources. Information on the size and distribution of the coherently scattering domains as well as the type, spatial arrangement, and density of dislocations can be readily obtained. For the dislocations, the Wilkens model [119] implemented in the PM2K software provides the total dislocation density ρ_D , the dislocation cut-off radius R_e related to the dislocation radius of influence, as well as a mixing parameter M giving the ratio between edge and dislocations. All of these are refinable parameters related to each active slip system in the material. For FCC crystals, the primary slip system is $\frac{1}{2} \{111\} \langle 110 \rangle$, with a Burgers vector of magnitude $a/2 \cdot 2^{-1/2}$, where a is the lattice parameter. The anisotropic effect of dislocations is embedded in the dislocation contrast factor C_{hkl} [120] computed from the single crystal elastic constants relative to the primary slip system [121]. For completeness, a brief comment about the relations between the computed values of the dislocation densities with the resulting yield stress based on the application of Taylor's hardening model is presented in the Supplementary Information file, section S3.

2.4. SEM imaging

Scanning electron microscopy (SEM) images were acquired using an SEM EVO 40 (Carl Zeiss Microscopy GmbH, Oberkochen, Germany) scanning electron microscope, equipped with an HKL Nordlys EBSD detector system (Oxford Instruments/HKL) for EBSD analyses. First, 4 mm thick cylinders were extracted with a diamond micro cutter from the 15 mm cylinders used for neutron texture mapping. The cylinders were then embedded in epoxy resin, single-side ground to 1200 grit with SiC abrasive paper and polished with diamond pastes down to $1 \mu\text{m}$. A mirror surface was obtained by final polishing using a $0.5 \mu\text{m}$ colloidal oxide suspension (Struers GmbH). Ultimately, the epoxy resin was mechanically removed before mounting the specimen on the SEM stub. SEM micrographs were acquired after etching with Glyceregia (60 s), at a magnification of 2.5 k to 50 k using an accelerating voltage of 20 kV at a working distance of 10 mm. The ImageJ freeware was used to analyse the SEM images. As shown in the Supplementary Information file, section S4, grey-scale intensity profiles have been analysed in several portions of each SEM image, exploiting the different contrast between cells' interior and boundary regions. From the intensity profiles, the width of the cell's interior and the thickness of the walls have been collected by measuring the distance between the half-height points of adjacent peaks and the FWHM (full width at half maximum), respectively. About 200 cells and 150 cell walls were measured for each specimen.

2.5. EBSD analysis

Electron backscattered diffraction is a popular technique capable of providing on a local scale both visual and quantitative information on microstructural properties such as crystallographic texture [122–124], grain size and morphology [125–127], distribution of geometrically necessary dislocations (GND) [55,128], strains [125,129] and recrystallization phenomena [130,131]. In this work, for the EBSD analysis, the samples were tilted by 70° and the microscope was operated at 25 kV, using a working distance of 12 mm. Low-resolution maps were acquired by sampling a 400×200 points grid at a magnification of $500\times$, using a step-size resolution of $1 \mu\text{m}$, thus probing a $400 \times 200 \mu\text{m}^2$ area in 7 h of continuous acquisition. Also, high-resolution maps were acquired by sampling a 400×180 points grid at a magnification of $500\times$, using a step-size resolution of $0.5 \mu\text{m}$, thus probing a $200 \times 90 \mu\text{m}^2$ area in 16 h of continuous acquisition. For data acquisition and indexing the HKL Flamenco software was used. For data post-processing, including grains reconstruction, computation of ODF, and GNDs visualization and quantification, the open-source MTEX toolbox installed in MATLAB (The MathWorks Inc., Natick, USA) was employed. Regarding grain reconstruction, a threshold angle of 9° was used to define high-angle grain boundaries (HAGBs), while a lower threshold angle of 1° was used to define low-angle grain boundaries (LAGBs). During grains reconstruction, those grains containing fewer than 5 pixels were excluded and incorporated, along with non-indexed pixels, into the nearest neighbouring grains, while a final denoising procedure was performed using a variational spline filter method. Importantly, all accepted EBSD data used for the analysis had a native indexing rate between 79% and 85%, to avoid excessive data manipulation.

3. Results

3.1. Cyclic elastoplastic tests

In Fig. 2, the cyclic EP response of the AISI 316L specimens versus the number of cycles, N , is represented by a subset of the hysteresis loops for the S-3000 specimen. The presence of hysteresis loops indicates the establishment of unrecoverable plastic damage, whose extent is proportional to the hysteresis area [46]. By inspection of Fig. 2, the loops area (i.e. the plastic damage) was not significantly affected by the

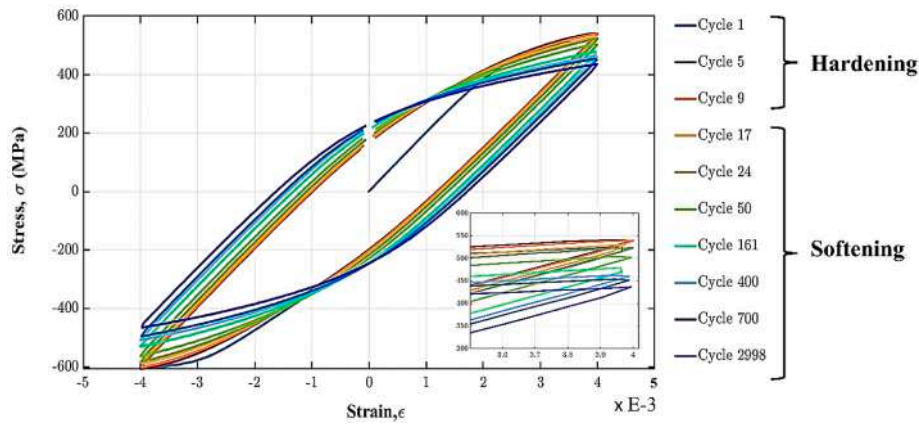


Fig. 2. Selected stress-strain curves for the 3000-cycled specimen (S-3000) showing the hardening and softening regimes. The inset displays a magnified view of the peak tensile stress for each cycle.

number of cycles, but a non-monotonic trend of compressive and tensile maximum stresses was observed, indicating changes in the materials microstructure, in agreement with the literature [53,54,132]. In fact, on increasing N, the stress-strain loops show a trend consisting of a primary modest hardening phase occurring within the first 7–9 cycles, followed by a softening regime at higher N. As reported in Fig. 3 A, during the hardening stage the positive peak stress $\sigma_{Max,Tensile}$, relative to the tension stage ($\epsilon > 0$), is increasing slightly from 525 ± 8 to 543 ± 7 MPa (about 3% increase), while it is decreasing to about 481 ± 9 MPa after 200 cycles and 440 ± 9 MPa after 3000 cycles as the specimen enters in its softening stage. A Similar behaviour is noticed in Fig. 3 B for the negative peak stress $\sigma_{Max,Compressive}$, relative to the compression stage ($\epsilon < 0$), but as $\sigma_{Max,Compressive}$ has a consistently higher absolute value than $\sigma_{Max,Tensile}$, the mean stress σ_{Mean} , defined as the mathematical average between the tensile and compressive peak stresses [133], results to be

moderately compressive. As shown in Fig. 3C, the σ_{Mean} gradually moves from the initial -39 ± 10 MPa towards less negative up to -15 ± 7 MPa by increasing N. Interestingly, a quasi-linear increase of σ_{Mean} with $\log_{10}(N)$ has been observed. Similarly, as reported in Fig. 3 D, the mean elastic modulus ΔE_{Cycle} decreased linearly with $\log_{10}(N)$, with comparable values of the rate $d(\Delta E_{Cycle})/d(\log_{10}(N))$. Importantly, as visible in all the panels of Fig. 3, the hardening-softening transition occurred at similar values of N for each tested specimen, with the slight differences due to intrinsic small variations among the individual specimens.

3.2. Neutron diffraction

3.2.1. RS analysis

As depicted in Fig. 4, only the uncycled specimen (S-AB) shows a parabolic RS distribution around the cylindrical axis, principally for the

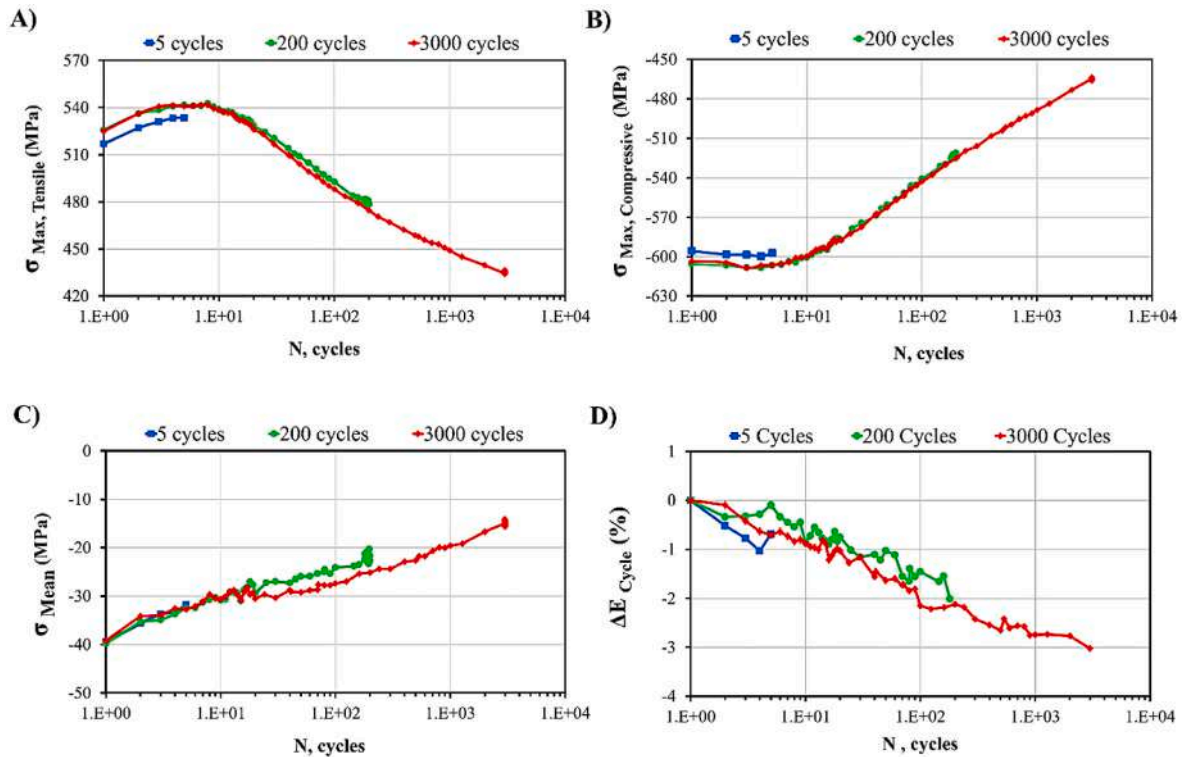


Fig. 3. (A) Maximum tensile stress, (B) maximum compressive stress, (C): mean stress, and (D) percentage variation of cyclic elastic modulus as a function of the number of LCF cycles.

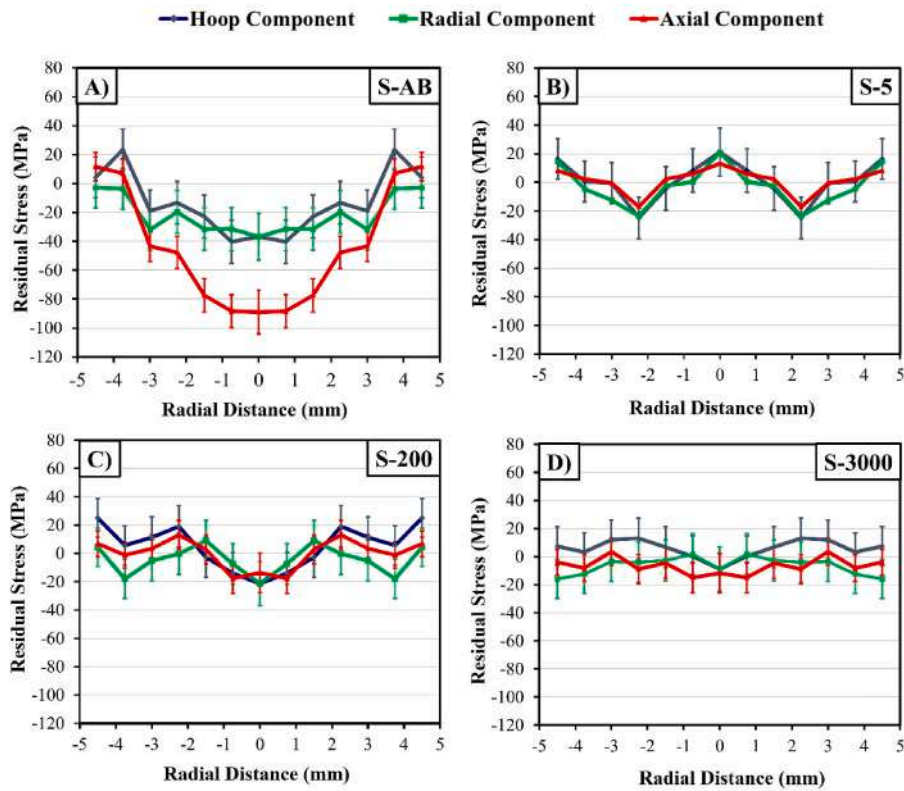


Fig. 4. Residual stress profiles calculated from ND data for A) S-AB, B) S-5, C) S-200, and D) S-3000. Error bars are determined by the averaging procedure assuming axial symmetry within the material.

axial component. By increasing the number of elastoplastic cycles, the RS distribution is changed and progressively smoothed out below the detection limit, estimated at around 15 MPa from the strain accuracy of 50 μ strain ($5 \cdot 10^{-5}$) based on the neutron counting statistics. It is evident that even after 5 LCF cycles, sample S-5, the stress distribution practically vanishes and remains practically null for higher cycling, S-200, and S-3000 samples. These findings suggest that the rapid flattening of RS can be due to the uniform overall plastic deformation (beyond the yield

strength) together with the microstructural rearrangements occurring within the material following the elastoplastic deformation. The latter is also reflected in some texture changes, as discussed below. For the sake of completeness, the RS distribution in the S-AB shows remarkably lower values than those typically reported in the literature [97,102,134]. The discrepancy could be due to a combination of factors including different process conditions, internal porosity, or heat treatments, but a thorough investigation in this direction goes beyond the aims of the present work.

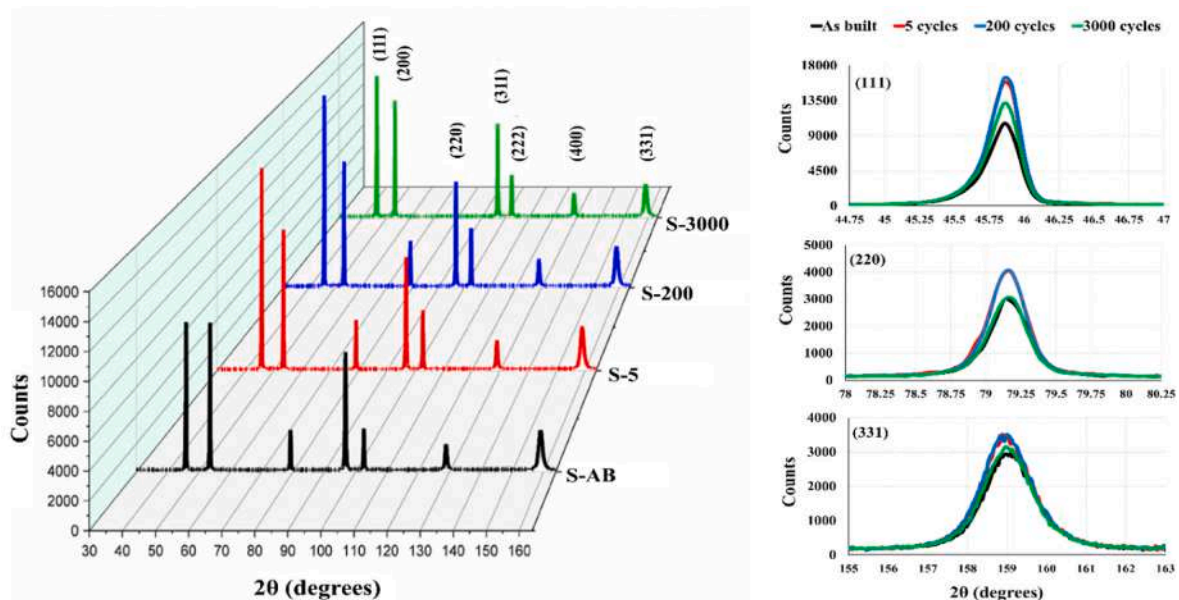


Fig. 5. (Left) Neutron diffraction profiles for the four specimens analysed and, (Right), a magnified view of selected reflections shows the change in peaks intensity and centre position with increasing elastoplastic cycles.

3.2.2. ND patterns and WPPM

Fig. 5 displays the diffraction patterns of the four tested specimens in the 2θ range 30–160°. Only the reflections associated with the austenitic phase are present, indicating the absence of pristine or mechanically induced martensite or ferrite phases. While the (200) and (311) reflections were unaffected by increasing N, some differences in relative peak height and no significant peak shift were observed among the different specimens for the (111), (220), and (331) reflections, as shown in the overlay of baseline-subtracted plots in Fig. 5 B. The difference in relative peak height suggests that the EP deformation affects the crystallographic orientation of grains and sub-granular structures, while the absence of significant peak shifts suggests that no macroscopic residual stresses are introduced. Interestingly, as shown by the overlaid plots in Fig. 5, the peak intensity of the (111), (110), and (331) reflections is increased for S-5 and S-200 and then is reversed for S-3000 to reach almost the same intensities as for S-AB, suggesting a non-monotonous impact of EP deformation on the crystallographic orientation spread.

The refined microstructural parameters obtained from the WPPM procedure are reported in Table 4, while the modelled patterns are represented in Fig. 6, overlaid with the corresponding experimental ND data and difference plot (residual). The best goodness of fit (GOF) reached for all the specimens was in the range of 1.75–2.23.

The resulting total dislocation density ρ_D ranged between 5.8 and 8.1 10^{-14} m^{-2} , in good agreement with the values typically reported in the literature for comparable strain amplitudes [135,136]. Correspondingly, the dislocations outer cut-off radius, Re , ranged between 88 and 49 nm. The ρ_D value first increases from S-AB to S-5, for which the largest ρ_D value was obtained, and then decreases continuously for S-200 and S-3000. Interestingly, the refined values for the fraction of edge dislocations, $\rho_{D, Edge}$, decreases monotonically from about 65 % to about 41%, suggesting a faster depletion of edge dislocations over screw dislocations throughout the cyclic EP deformation, contrary to what is typically observed for static strain [137].

The particle size broadening contribution was modelled by a lognormal distribution of cylinders, with refinable parameters being the diameter D and the average aspect ratio D/L , with L being the cylinder length. In metals and alloys, as discussed by Muránsky et al. [55], small misorientations between areas separated by dislocation cells and LAGBs create domains that have a continuous spectrum of misorientations which are represented by size broadening in diffraction peaks. To provide reasonable initial values for the crystallite size broadening, the size of characteristic solidification cells was measured from SEM micrographs, such as the one shown in Fig. 7. In Fig. 7 B–C fibre-like solidification cells with the axis aligned parallel to the build direction or transversal to it can be noticed, respectively. The average and standard deviation of cell width (CW) and cell wall thickness (WT) are reported in Table 5. No significant variations in the characteristic cells cross-sections are induced by the applied EP deformation. As shown in the Supplementary Information file, section S4, the distribution of the cells' diameter was approximately lognormal. Therefore, to represent the fibre-like morphology of the solidification structures in the fitting process, a lognormal distribution of cylinders was employed, using an initialised value of D corresponding to the average $\langle CW \rangle$. It is worthwhile mentioning here that for all samples, the contribution of size effects to the observed peak broadening was negligible compared to the dislocation-related one. Errors in the size estimation become easily large for crystallites exceeding ca. 100 nm [138]. Consequently, the

refined size values reported in Table 4 should be interpreted just as a reference estimate.

Fig. 8 shows as a function of N the values of the average peak tensile stresses, σ_{Max} , the total dislocation density, ρ_D , and the microstrain ϵ_p computed through the Ashby equation [139,140]:

$$\epsilon_p = 4 * b * \lambda * \rho_D \quad \text{Equation 3}$$

where the Burgers vector $b = 0.254 \text{ nm}$ is the Burgers vector relative to the $\frac{1}{2} \{111\} \langle 110 \rangle$ slip system, calculated from the refined lattice parameter value of 0.3595 nm, and λ is the mean spacing between obstacles to dislocation motion, here equal to the cell width, $\langle CW \rangle$. While proceeding with the cyclic EP deformation, ρ_D first increases during the first few EP cycles and then gradually diminishes. Notably, the trend of ρ_D reproduces very closely with the one of σ_{Max} recorded during the LCF tests. Also, given the similar $\langle CW \rangle$ values among the different specimens, the trend of ϵ_p follows that of ρ_D .

In Fig. 8, the σ_{Max} and $\delta\sigma_{Max}$ values for the S-AB (0 cycles series) are respectively the mean value and error calculated by averaging the σ_{Max} values of the loaded specimens after the first cycle. Second, the values of σ_{Max} and $\delta\sigma_{Max}$ at a certain N are taken by averaging over the measured values at equivalent N for the three loaded specimens, while for ρ_D the error values $\delta\rho_D$ are taken by averaging over repeated fits with different initialising values. For microstrain, the errors are calculated by standard error propagation procedure.

3.2.3. Texture analysis

The evolution of texture with the number of EP cycles can provide additional information on the microstructural contribution to stress relaxation and mechanical behaviour. Fig. 9-A reports the pole figures (PF) for the (111), (200), (220), and (311) reflections for the four specimens, while Fig. 9-B shows the texture coefficients J_{ODF} defined according to Equation 2.

$$J_{ODF} = \int |f(g)|^2 dg$$

As shown in Fig. 9 A, all specimens show a preferential (220)-fibre orientation parallel to the build direction, as evidenced by the maximum intensity at the centre of the (220) pole figure, while the (200) orientations are parallel to the scanning directions on the x-y plane perpendicular to the build direction, a condition typical for LPBF stainless steels [134,141]. Interestingly, a counterintuitive evolution of texture with increasing N can be observed in Fig. 9 A. Already after the first 5 cycles (S-5), the PFs change notably from the as-built condition (S-AB). In particular, due to the axial symmetry of the applied load during the LCF tests, some degree of cylindrical symmetry is attained, as demonstrated by the appearance of circular patterns in the PFs (see Fig. 9 A, S-5 column) indicating that the crystallites have a preferred tilt to the corresponding direction, but lack of in-plane orientation [142]. Additionally, a J_{ODF} reduction of about 14% was observed for sample S-5 as far as the as-built condition, S-AB, is concerned (Fig. 9 B), apparently due to the development of the (110)-fibre texture component at the expense of the pronounced central peak observed in the as-built condition. This fibre-type texture is mostly retained for S-200, but it is significantly lost for S-3000, for which the PFs pattern and J_{ODF} value approach those of the as-built condition, sample S-AB.

Table 4

Refined microstructural parameters from the WPPM data analysis, with δ being the estimated standard deviation (esd).

Specimen	$\rho_D \times 10^{14} [\text{m}^{-2}]$	$\delta\rho_D \times 10^{14} [\text{m}^{-2}]$	Re [nm]	δRe [nm]	$\rho_{D, Edge}$ (%)	$\delta\rho_{D, Edge}$ (%)	L [nm]	δL [nm]	L/D	D [nm]
S-AB	7.31	0.14	52.1	4.32	65.7	0.80	122.1	39.1	0.62	198.6
S-5	8.08	0.18	49.0	4.05	58.9	0.42	222.1	72.2	0.74	300.1
S-200	6.71	0.08	66.4	0.72	43.9	1.97	185.9	54.1	0.44	422.5
S-3000	5.84	0.09	88.3	2.47	41.2	2.04	217.1	28.4	0.55	394.6

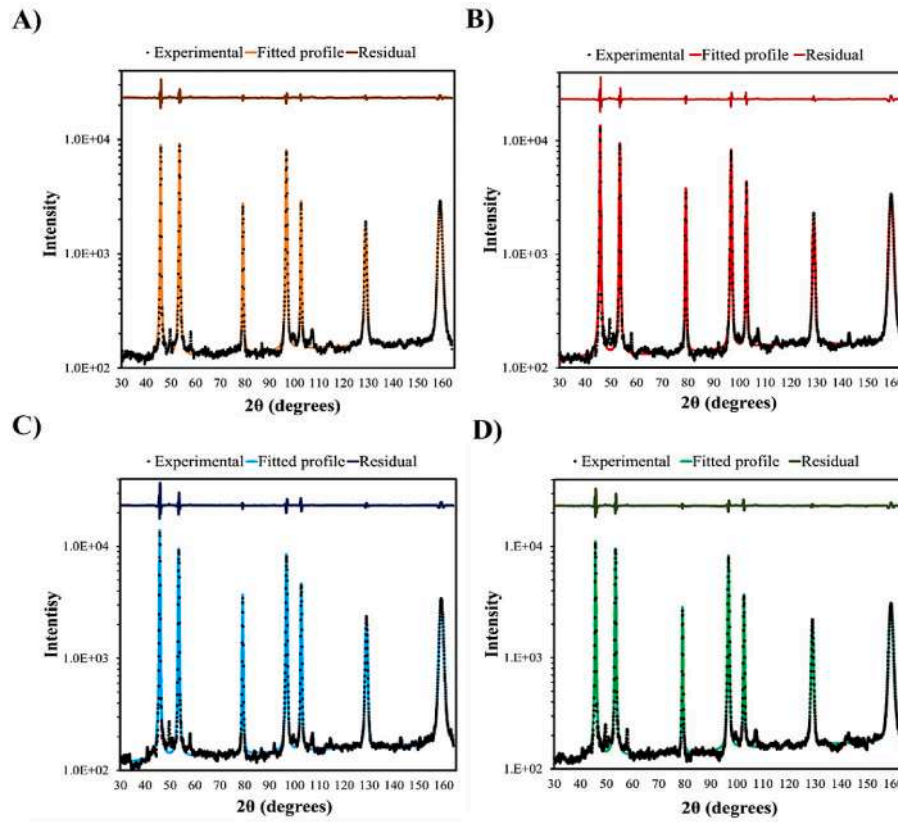


Fig. 6. WPPM fit results for A) S-AB, B) S-5, C) S-200, and D) S-3000 specimens. Black dots are experimental data while the superimposed coloured curves are the fitted profiles. Above all patterns, it is reported the fit residual. The intensity axes are in logarithmic scale.

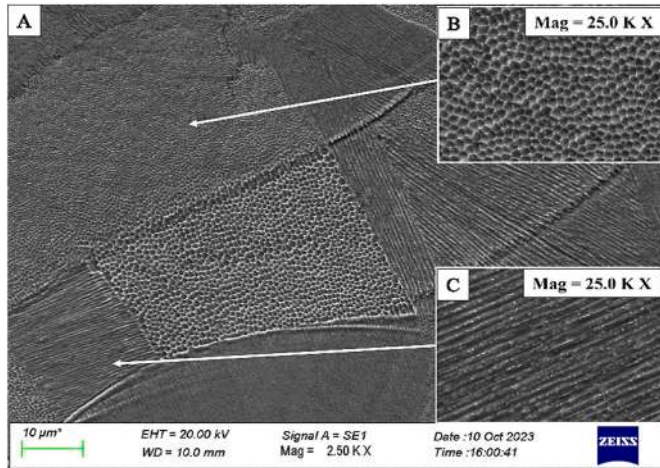


Fig. 7. SEM micrograph of a portion of the etched surface of S-3000, showing the typical columnar microstructure of LPBF AISI 316L. Inserts B and C show higher magnification of cells aligned parallel and perpendicular to the surface normal direction, respectively.

Table 5

Average dimension of cell widths (CW) and wall thickness (WT) for the four specimens, with standard deviations δ .

Specimen	<WT> (nm)	δ_{WT} (nm)	<CW> (nm)	δ_{CW} (nm)
S-AB	62.8	11.2	339.3	67.8
S-5	77.4	12.7	385.61	80.39
S-200	78.9	20.1	373.36	46.8
S-3000	81.2	15.3	391.7	70.6

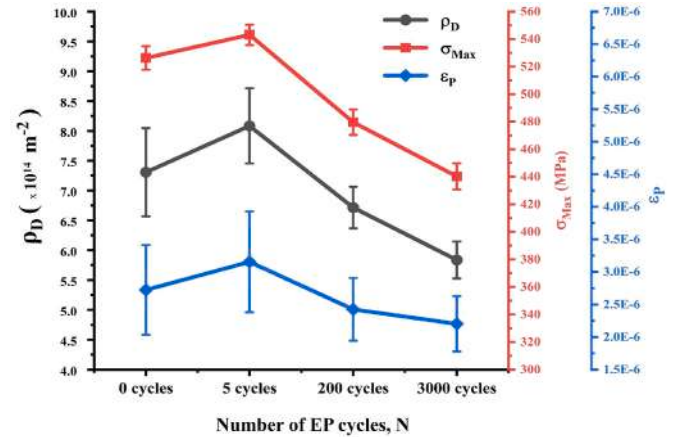


Fig. 8. Comparison between the trends of dislocation density ρ_D , computed with PM2K from neutron diffraction data using the Wilkens model, the peak tensile stress σ_{Max} measured from the LCF tests, and Ashby's plastic microstrain against ϵ_P against the number of elastoplastic (EP) cycles.

3.3. EBSD analysis

3.3.1. Grains reconstruction

Grains-reconstructed, low-resolution EBSD inverse pole figure (IPF) maps (step-size of 2 μm) taken on polished cross-sectional cuts are reported in Fig. 10. According to the reported IPF-Z colour key map, most of the grains in all the IPF maps show a preferential alignment of grains along [110], in good agreement with the PF maps acquired via neutron diffraction and reported in Fig. 9 A. The grains orientation follows the typical behaviour of FCC metals grown by MAM processes, with

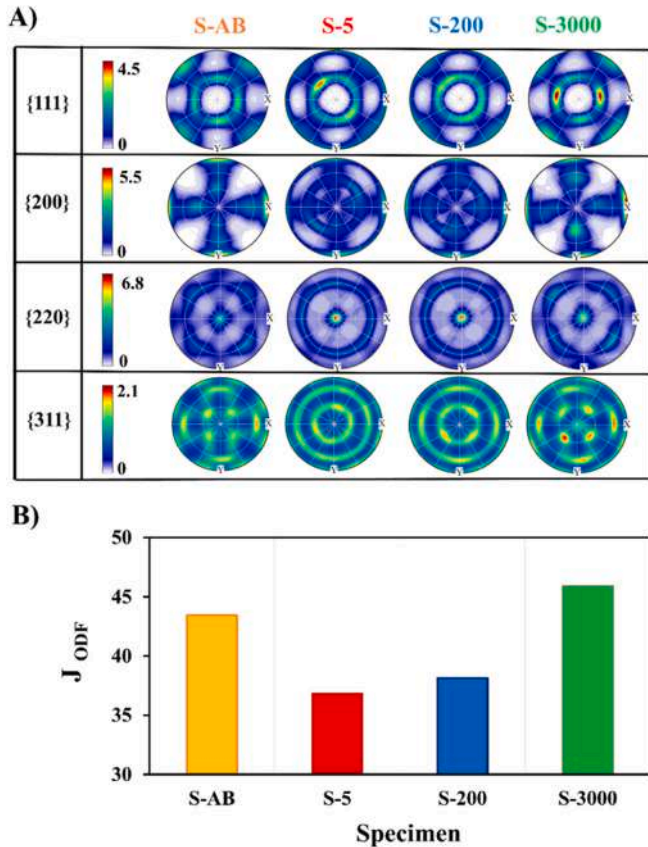


Fig. 9. Neutron diffraction pole figures for the four $\{hkl\}$ reflections, the centre of the PF corresponding to the building direction; B): Texture coefficients calculated using Equation (2).

crystallographic directions parallel to the build direction being between the $[110]$ and the $[100]$ directions, with only a fraction of the grains orienting towards $[111]$.

In Fig. 11 there are reported the distribution of grain boundary (GB) misorientation angles (left column) and the distribution of grains equivalent diameters D_{eq} (right column), defined as the diameter of a circle with the same area of the grain. Also, the kernel average distribution (KAD) curves are superimposed on each distribution to highlight the relevant underlying contributions. For both series, a common trend is visible, consisting of a gradual increase of the KAD intensity at low values of both GB misorientation angle and D_{eq} , suggesting a partial and gradual grains fragmentation with increasing N . This grain fragmentation has been characterized more quantitatively by fitting the KAD curves of each specimen with a suitable number of Gaussian curves representing the main grain populations. The number of Gaussian contributions used was deduced by the profile shape of the KAD curves in Fig. 11, right column. The complete fit results are reported in the Supplementary Information, section S5, while the main information is reported in Table 6.

Based on the peak position of the best-fitting Gaussian contributions, grains populations were arbitrarily classified into small grains (SG), medium grains (MG), large grains (LG), and ultra-large grains (ULG), with a D_{eq} of about 2 μm , 10 μm , 25 μm , and 70 μm respectively. While SG, MG, and LG populations were observed for all the specimens, ULG contribution was not detected on the S-AB maps.

As shown in Table 6, the mean D_{eq} and relative abundance of each population are affected by the number of loading cycles. Concerning the grain size, the mean D_{eq} of SG is increasing by almost 13%, after 5 cycles, then by a further 8% after 200 cycles. Such an increase in SG comes at the expense of larger grains. For MG, whose D_{eq} is reduced by about

17% after 5 cycles, and then substantially stabilizes. The D_{eq} of LGs is decreasing by 12% after 5 cycles and then by a further 3% after 200 cycles and another 3% after 3000 cycles. Eventually, the D_{eq} of ULG is decreasing by 7% between 5 and 200 cycles and by another 7% after 3000 cycles. As for the relative abundancies, the fraction of the fitted SG contribution to the total KAD changes from 17 to 18% for the as-built and 5-times cycled specimens to about 27–28% for the specimens tested for 200-to-3000 cycles, with an average increase of about 40%. Correspondingly, the fraction of MG decreases from around 73% for the as-built specimen to 62–61% for S-5 and S-200, corresponding to a 16% reduction, and then to about 57% for S-3000, corresponding to a further decrease of about 7%. Also, while the fraction of ULG decreases from about 3% to 1% from S-5 and S-3000, the absence of a trend for LG abundancies with N could be due to the intrinsic differences amongst the specimens.

3.3.2. GND analysis

Local misorientations are quantified by the kernel average misorientation (KAM) [143] and are strictly correlated to the presence of GND. Fig. 12 shows the high-resolution IPF maps (panels A1-D1), the GND distribution maps (panels A2-D2), and the KAM maps of the same areas. The IPFs are referenced to the same IPF-Z as the low-resolution IPF maps reported in Fig. 10. By comparing panels A2 (specimen S-AB) with B2-D2 (specimens S-5, S-200, and S-3000), it emerges that the GND distribution is affected by the loading. While the majority of GND is accumulated at LAGBs and HAGBs in S-AB (Fig. 12 A1), for cycled specimens the density of intragranular GND is enhanced, and their spatial arrangement is also changed Fig. 12 A2-A4.

The mechanically induced intragranular migration and rearrangement of GND due to the activations of slip mechanisms lead to the formation of organized dislocation structures [53] consisting of a network of low GND density regions 300–500 nm wide delimited by interconnected boundary walls of high GND density [23,143]. The KAM values of these high GND density walls are typically in the range of 1–2° [18,83]. These values of GNDs and KAM observed in Fig. 12 A2-D2 are in good agreement with the literature. Relatively large GND densities on the order of 1–5 10^{15} m^{-2} are accumulated at the boundaries of these structures, surrounding low GND densities regions of about 1–3 10^{14} m^{-2} . Interestingly, such structures are absent in the IPF map of S-AB, with high GND density regions occurring only at LAGBs. As discussed by Liu et al. [135], during plastic deformation dislocations located at grain boundaries are pumped from the boundaries towards the grains' interior. In the present work, this effect is suggested by inspection of Fig. 12 A2-D2, where intricate arrays of GND are developed within multiple grains, especially within grains with a crystallographic orientation tending or approximately parallel to the $\langle 100 \rangle$ direction (cf. the IPF-Z colour map in Figs. 10 and 12). Some further analysis of the GND distributions is reported in the Supplementary Information file, section S6.

4. Discussion

This study demonstrates how the microstructure of LPBF 316L steels undergoes significant changes during cyclic EP deformation when crossing the hardening-softening transition. In the following, an effort is made to establish correlations between certain microstructural analysis findings and the observed mechanical responses.

4.1. Residual stress and cyclic mean stress

Residual stresses in the as-built specimens are introduced by the thermal history of the LPBF process. The rapid elimination of RS within the first EP cycles (Fig. 4) can be explained by considering the effects of plastic deformation, as proved by the microstructural modifications detected by the textural changes and rearrangement of dislocation structures. At the grain-scale level, the periodic inversion of the deformation direction and the reorganisation of dislocations into low-energy

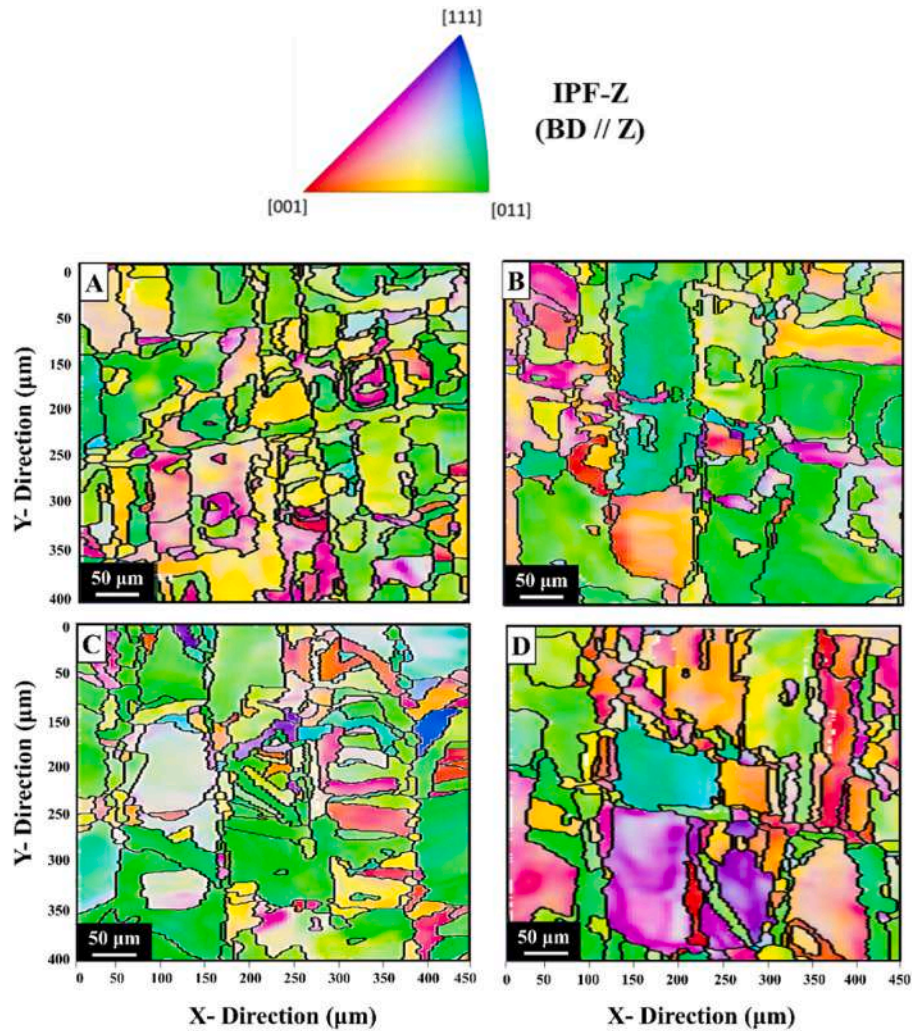


Fig. 10. EBSD inverse pole figure (IPF-Z) maps for A) as built, B) S-5, C) S-200, and D) S-3000 specimens. The colour key IPF map is reported on the top along with the reference specimen direction. (For interpretation of the references to colour in this figure legend, the reader is referred to the Web version of this article.)

cellular configurations prevent the build-up of back stresses which is typically encountered during uniaxial tensile deformation owing to the pinning of dislocations at Mo and Cr segregated atoms within the cellular walls [132,144,145]. The poor back-stress accumulation is therefore not sufficient to compensate for the stress dissipation perpetrated through the plastic-strain effects, leading to the observed RS relaxation [71,146].

Contrarily to RS, the cyclic mean stress σ_{Mean} changes slowly, with its absolute value decreasing linearly with $\log_{10}N$ (Fig. 3 D). This slow change of σ_{Mean} can be correlated with the change in back stress magnitudes occurring during the cyclic EP deformation [53]. For the specimen cycled until failure, the linear increase extended throughout the whole deformation, passing from compressive to tensile values (data not shown). This suggests that albeit the solidification-induced RS are removed in the early stages of the cyclic EP deformation, the compressive internal stresses originated by other sources during the fabrication process are only gradually reduced, probably because of the concurrent accumulation of tensile stresses upon cycling.

4.2. Evolution of dislocations arrangements and grain size

Bahl et al. [87] clarified the dominant role of dislocations over grain size in determining the mechanical strength of LPBF 316L stainless steels under tensile tests, attributing this to the poor capabilities of LAGBs to provide sufficient hindrance to dislocation motion across grains. In the

present study, any size hardening contribution delivered by grain refinement (Fig. 11 and Table 6) as predicted by the Hall-Petch rule is largely outperformed by the effects of dislocations rearrangement. The size-hardening effect is grounded on the piling-up of dislocations at misoriented grains or cell boundaries. Given that, a large fraction of grains are several microns in size (Fig. 11), and that the misorientation at the cells boundaries is about 2° (see EBSD maps of Fig. 12 A3-D3), size-hardening cannot compensate for the softening mediated by the partial depletion and reorganisation of dislocations. This is further supported by the WPPM analysis performed on the neutron diffraction data (Fig. 8), showing a clear correlation between dislocation density and peak stresses despite the very small variation in grain size distribution. The organization of dislocations into cellular structures is visible in the GND maps in Fig. 12 A2-D2 and is probably the main mechanism of dislocation depletion which leads to the softening deformation stage.

4.3. Effect of dislocation arrangements and texture

The trends of total dislocation density and peak stresses (Fig. 8) can also be correlated with the PFs distributions (Fig. 9-A) and texture strength coefficients (Fig. 9 B). As discussed by Pham et al. [142], texture can result in specific crystallographic orientations (single or multiple peak-type texture) or multiple orientations within the specimen having an axial symmetry (fibre-type texture), the latter indicating a preferential growth angle to the normal, but lack of in-plane orientation.

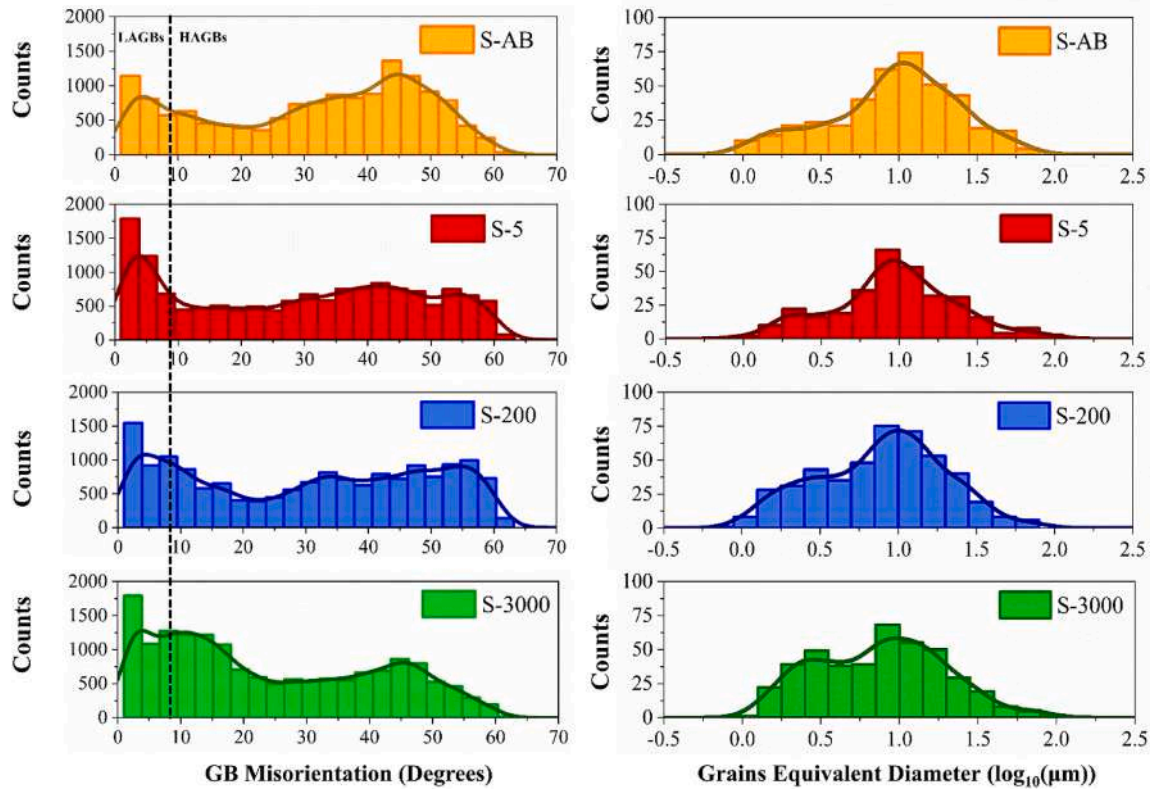


Fig. 11. (Left) distribution of misorientation angle at grain boundaries (GB) with the evidenced threshold between LAGBs and HAGBs and (Right): distribution of grain equivalent diameter versus the number of EP cycles.

Table 6

Fitted values of equivalent diameter (D_{eq}) and fraction for the populations of small grains (SG), medium grains (MG), large grains (LG), and ultra-large grains (ULG).

Specimen	SG D_{eq} (μm)	SG Fraction (%)	MG D_{eq} (μm)	MG Fraction (%)	LG D_{eq} (μm)	LG Fraction (%)	ULG D_{eq} (μm)	ULG Fraction (%)
S-AB	2.0	17.1	11.0	72.6	28.7	10.3	ND	ND
S-5	2.3	17.7	9.2	61.8	25.3	17.0	65.7	3.5
S-200	2.5	28.3	9.6	60.9	24.4	9.8	70.4	1.0
S-3000	2.4	27.5	9.2	56.6	23.6	14.8	75.4	1.1

According to Fig. 9 A, S-AB shows a peak-type texture with two dominant peak components which are rotated by 90° to each other around the BD, and prone to form a (220)-fibre component. The corresponding PF distributions of S-5 show a much more pronounced angular symmetry around the BD, forming rings around the central axis. At the same time, the (220) crystallographic direction remains well aligned to the BD throughout the EP tests, confirming the establishment of a (220)-fibre texture. At this point in the EP deformation, the dislocations reach the highest density and start to form cellular structures. As the number of cycles increases, S-200 and S-3000, along with the progressive reduction of dislocation density and stabilization of the cellular arrangements, the fibre texture gradually returns to a peak-like pattern resembling that of the initial condition, S-AB.

The interpretation of the observed texture evolution is not trivial. While the formation of axial texture within the first stages of the EP deformation is expected according to the axial symmetry of the plastic deformation, the reversion to the initial texture after 3000 EP cycles seems counterintuitive. One plausible explanation is based on some

“texture memory” effect. During the first cycles, the mechanically induced enhancement of dislocations results in the enhancement of maximum stresses (i.e., the hardening) and the establishment of a fibre-type texture. This higher texture uniformity facilitates the motion and reorganisation of dislocations into cellular structures with a high number of LAGBs, which facilitate the reabsorption of dislocations and the following mechanical softening. Later in the deformation process, the exposure to multiple EP cycles is probably responsible for the suppression of certain angular orientations around the specimen axis, while other components are retained or even strengthened, resulting in the restoration of the peak-like texture at the expense of the fibre texture.

Alternatively, the unexpected texture shown by S-3000 could be attributed to inconsistencies in individual sample printing processes. In this regard, preliminary Neutron Tomography investigations performed on cycled specimens revealed the presence of small porosities ($\approx 1\%$ volume, data not reported) in all specimens. It is then possible that with increasing N, inherent defects introduced during the printing process might have served as local stress concentrators, facilitating the

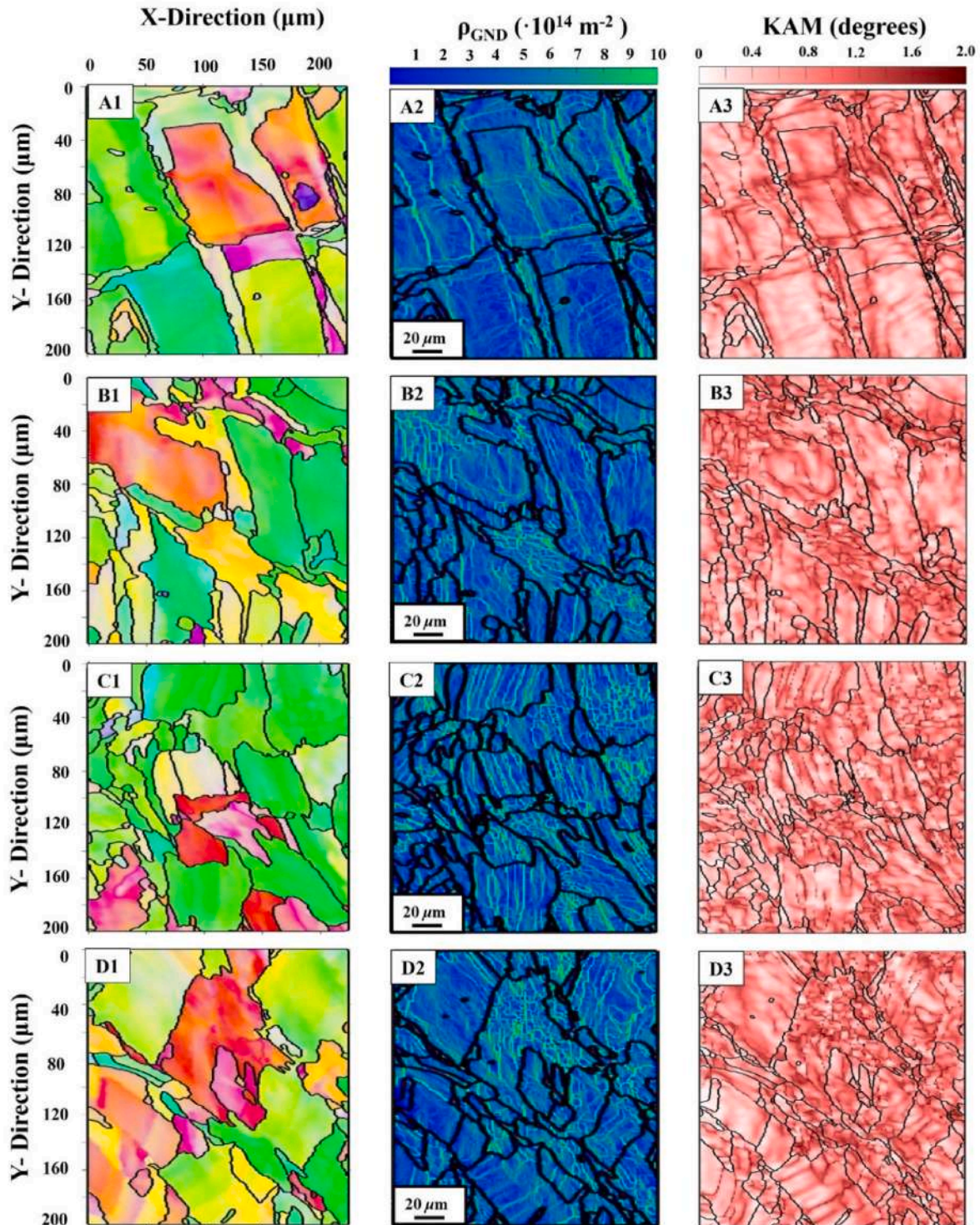


Fig. 12. IPF maps (panels A1-D1) and the corresponding GND density (panels A2-D2) and KAM (panels A3-D3) maps computed with MTEX. The colour-key of the IPF maps is referred to the same configuration used in Fig. 10. The scale bar in panels A2-D2 is the same for all other panels. (For interpretation of the references to colour in this figure legend, the reader is referred to the Web version of this article.)

development of defect structures such as cracks and voids [46,147]. In this framework, a higher initial porosity in S-3000 might have promoted the development of more defect structures, enabling it to accommodate non-plastic straining without altering its texture, while still exhibiting RS relaxation. This might also explain the low GND density observed via EBSD, and the low total dislocation density computed via ND analysis. However, although the development of such defect structures could

account for the continuous decline of E_{cycle} observed in Fig. 3 D, one might expect a faster decline of the E_{cycle} for S-3000 if it hosted a larger number of these defects, due to the smaller resistant section. Contrary to this expectation, the reduction rate of E_{cycle} with N for the S-3000 is comparable to that of the other specimens (Fig. 3 D). Therefore, this observation challenges the assumption of a significantly larger volume of defects in that specific specimen.

As a final remark, accounting for the presence and development of defect structures can help explain the lack of correlation between texture and stiffness evolutions. As shown in Fig. 9 B, the change in the type of texture (from peak to fibre) causes a decrease in the texture coefficient J_{ODF} , indicating a higher degree of crystallographic coherence. While such a change in J_{ODF} may influence the macroscopic stiffness E_{cycle} due to mechanical anisotropy in polycrystals, this study did not identify significant correlations between the two. By increasing N , E_{cycle} is decreasing monotonically while J_{ODF} is first decreasing during the hardening and then increasing during the softening. This lack of correlation can be explained by the small variation in texture coefficient. As discussed by Kamaya [148], macroscopic stiffness can be regarded as the volume average of the single-crystal elastic constants of polycrystalline materials along the direction of applied stress. While the large change of texture, i.e., of the relative amounts of crystallographic orientations, is expected to yield large variations in macroscopic stiffness, in this work such texture difference is small. Therefore, for the specimens tested in this work, it is possible that the formation of microporosities and cracks was more determinant for the continuous decay of E_{cycle} .

5. Conclusions

In this study, the effects of cyclic EP deformation on the microstructural characteristics and macroscale residual stress evolution of LPBF AISI 316L stainless steel were studied as a function of the number of deformation cycles, using neutron diffraction methods and EBSD. The cyclic EP response showed the bimodal hardening-softening behaviour typical for LPBF austenitic SS, with the hardening-softening transition being the focus of the present investigation. Our results suggest that the density and arrangement of dislocations are the primary microstructural parameters influencing the plastic resistance of LPBF SS under cyclic EP loading. Notably, we observed a seamless agreement between the trend of dislocation density and peak stresses, suggesting a close correlation between the two phenomena. Concerning the RS, these vanished within a few cycles in the hardening region, implying a minor contribution to the overall fatigue life. However, RS might still play a role in determining the onset of the H-S transition. Therefore, excessive emphasis on RS control when designing LPBF processes for applications involving EP deformations (e.g., LCF regime), might be unnecessary. Instead, strict control over dislocation populations and texture attributes appears to be more significant, especially considering the present condition of low initial RS (<100 MPa) built up because of specific LPBF process parameters, while it cannot be excluded that higher initial RS values introduced by different process conditions might, in principle, evolve differently.

The specimens' texture reflected the microstructural changes occurring throughout the investigated deformation regime. Dislocations rearrangement and grain refinement mechanisms, along with promoting RS dissipation, were also responsible for establishing the fibre-like texture during the initial EP cycles. With cumulating cycles, although no remarkable further developments in dislocation rearrangement or grain refinement were detected, the increasing number of low-value HAGBs suggested a persistent modification of the microstructure. This was reflected in the loss of the fibre-like texture and recovery of a peak-like texture. It has been highlighted how the mechanically induced microstructural modifications had a feedback effect on the mechanical response. The hardening region occurred due to grain refinement, the formation of dislocation sub-structures, and an increase in the total dislocation density. Then, across the H-S transition, the initial rotation of grains yielded the fibre-like texture, facilitating the movement of dislocations along the specimen axis and their depletion at grain boundaries, resulting in lower resistance to plastic deformation during the softening phase.

In conclusion, starting from the results of the present study, further research could focus on improving the understanding of local damaging mechanisms of LPBF 316L stainless steel, considering representative

micro-structures such as dislocation structures. For instance, these results provide a basis for a follow-up study in which 3D microstructural changes during cyclic EP deformation can be used to model the fatigue behaviour within a Crystal Plasticity framework, aiming at refining and customizing LPBF processes to meet specific application requirements.

CRedit authorship contribution statement

Marco Beltrami: Writing – review & editing, Writing – original draft, Visualization, Methodology, Investigation, Formal analysis. **Marco Pelegatti:** Investigation, Data curation. **Michele Magnan:** Resources, Investigation. **Alex Lanzutti:** Resources. **Maxim Avdeev:** Resources, Investigation, Formal analysis. **Vladimir Luzin:** Writing – original draft, Validation, Resources, Investigation, Formal analysis. **Matteo Leoni:** Writing – original draft, Validation, Software, Resources. **Francesco De Bona:** Investigation, Funding acquisition. **Enrico Salvati:** Validation, Supervision, Resources, Project administration, Methodology, Funding acquisition.

Declaration of competing interest

Nothing to declare.

Data availability

Data will be made available on request.

Acknowledgements

This work has been supported by the following projects: “CONCERTO – Multiscale modelling/characterisation and fabrication of nano-composite ceramics with improved toughness” funded by the MUR Progetti di Ricerca di Rilevante Interesse Nazionale (PRIN) Bando 2020, Italy – grant 2020BN5ZW9; “NutShell - NUmberical modelling and opTimisation of SHELL Structures Against Fracture and Fatigue with Experimental Validations” funded by the MUR Progetti di Ricerca di Rilevante Interesse Nazionale (PRIN) Bando 2022, Italy – grant 20229BM9EL. The authors thank Eng. F. Sordetti, for executing the mechanical testing, and Prof. L. Fedrizzi, head of the laboratory of material science and engineering in the Polytechnic Department of Engineering and Architecture (DPIA) of the University of Udine, for the use of the scientific equipment (MTS, GDOES, and SEM + EDXS + EBSD).

Appendix A. Supplementary data

Supplementary data to this article can be found online at <https://doi.org/10.1016/j.msea.2024.146416>.

References

- [1] U.M. Dilberoglu, B. Gharehpapagh, U. Yaman, M. Dolen, The role of additive manufacturing in the era of Industry 4.0, *Procedia Manuf.* 11 (June) (2017) 545–554, <https://doi.org/10.1016/j.promfg.2017.07.148>.
- [2] M. Salmi, Additive manufacturing processes in medical applications, *Materials* 14 (1) (2021) 191–207, <https://doi.org/10.3390/ma14010191>.
- [3] W.J. Sames, et al., The metallurgy and processing science of metal additive manufacturing, *Int. Mater. Rev.* 61 (5) (2016) 315–360, <https://doi.org/10.1080/09506608.2015.1116649>.
- [4] A. Vafadar, F. Guzzomi, A. Rassau, K. Hayward, Advances in metal additive manufacturing: a review of common processes, industrial applications, and current challenges, *Appl. Sci.* 11 (3) (2021) 1–33, <https://doi.org/10.3390/app11031213>.
- [5] W.E. Frazier, Metal additive manufacturing: a review, *J. Mater. Eng. Perform.* 23 (6) (2014) 1917–1928, <https://doi.org/10.1007/s11665-014-0958-z>.
- [6] M. Karmuhilan, S. Kumanan, A review on additive manufacturing processes of inconel 625, *J. Mater. Eng. Perform.* 31 (4) (2022) 2583–2592, <https://doi.org/10.1007/s11665-021-06427-3>.
- [7] M. Laleh, et al., Progress in materials science, *Prog. Mater. Sci.* 133 (April) (2021) 101051, <https://doi.org/10.1016/j.pmatsci.2022.101051>.

- [8] J. Schröder, et al., Texture-based residual stress analysis of laser powder bed fused Inconel 718 parts, *J. Appl. Crystallogr.* 56 (4) (2023) 1–15, <https://doi.org/10.1107/s1600576723004855>.
- [9] S. Gao, et al., Additive manufacturing of alloys with programmable microstructure and properties, *Nat. Commun.* 14 (2023) 1–11, <https://doi.org/10.1038/s41467-023-42326-y>.
- [10] J. Chen, et al., Dynamic mechanical properties of 316L stainless steel fabricated by an additive manufacturing process, *J. Mater. Res. Technol.* 11 (2021) 170–179, <https://doi.org/10.1016/j.jmrt.2020.12.097>.
- [11] H. Bao, S. Wu, Z. Wu, G. Kang, X. Peng, P.J. Withers, A machine-learning fatigue life prediction approach of additively manufactured metals, *Eng. Fract. Mech.* 242 (September 2020) (2021) 107508, <https://doi.org/10.1016/j.engfractmech.2020.107508>.
- [12] W. Beard, R. Lancaster, J. Adams, D. Buller, *Fatigue Performance of Additively Manufactured Stainless Steel 316L for Nuclear Applications*, 2019, pp. 2144–2155.
- [13] V.B. Vukkum, R.K. Gupta, Review on corrosion performance of laser powder-bed fusion printed 316L stainless steel: effect of processing parameters, manufacturing defects, post-processing, feedstock, and microstructure, *Mater. Des.* 221 (2022) 110874, <https://doi.org/10.1016/j.matdes.2022.110874>.
- [14] P. Bajaj, et al., Steels in additive manufacturing: a review of their microstructure and properties, *Mater. Sci. Eng.* 772 (October 2019) (2020), <https://doi.org/10.1016/j.msea.2019.138633>.
- [15] S. Gorsse, C. Hutchinson, M. Gouné, R. Banerjee, Additive manufacturing of metals: a brief review of the characteristic microstructures and properties of steels, Ti-6Al-4V and high-entropy alloys, *Sci. Technol. Adv. Mater.* 18 (1) (2017) 584–610, <https://doi.org/10.1080/14686996.2017.1361305>.
- [16] J.S. Novak, M. Pelegatti, E. Kamenar, S. Zelenika, F. De Bona, “Experimental investigation of mechanical properties of the AISI 316L stainless steel: macro- and microscale,” *European Society for Precision Engineering and Nanotechnology, in: Conference Proceedings - 23rd International Conference and Exhibition, EUSPEN 2023*, 2023, pp. 67–70. June.
- [17] M.S. Pham, B. Dovggy, P.A. Hooper, Twinning induced plasticity in austenitic stainless steel 316L made by additive manufacturing, *Mater. Sci. Eng., A* 704 (July) (2017) 102–111, <https://doi.org/10.1016/j.msea.2017.07.082>.
- [18] Y.M. Wang, et al., Additively manufactured hierarchical stainless steels with high strength and ductility, *Nat. Mater.* 17 (October) (2017) 63–71, <https://doi.org/10.1038/NMAT5021>.
- [19] J. Schröder, et al., Understanding the impact of texture on the micromechanical anisotropy of laser powder bed fused Inconel 718, *J. Mater. Sci.* 57 (31) (2022) 15036–15058, <https://doi.org/10.1007/s10853-022-07499-9>.
- [20] O. Andreau, et al., Texture control of 316L parts by modulation of the melt pool morphology in selective laser melting, *J. Mater. Process. Technol.* 264 (August 2018) (2019) 21–31, <https://doi.org/10.1016/j.jmatprotec.2018.08.049>.
- [21] P. Tao, H. Li, B. Huang, Q. Hu, S. Gong, Q. Xu, The crystal growth, intercellular spacing and microsegregation of selective laser melted Inconel 718 superalloy, *Vacuum* 159 (October 2018) (2019) 382–390, <https://doi.org/10.1016/j.vacuum.2018.10.074>.
- [22] M. Smid, D. Koutny, M. Jambor, Z. Chlup, L. Nahlik, M. Jambor, Cyclic behaviour and microstructural evolution of metastable austenitic stainless steel 304L produced by laser powder bed fusion, *Addit. Manuf.* 68 (2023), <https://doi.org/10.1016/j.addma.2023.103503>.
- [23] K.M. Bertsch, G. Meric de Bellefon, B. Kuehl, D.J. Thoma, Origin of dislocation structures in an additively manufactured austenitic stainless steel 316L, *Acta Mater.* 199 (2020) 19–33, <https://doi.org/10.1016/j.actamat.2020.07.063>.
- [24] A. Heidarzadeh, J. Zava, Dynamic recrystallization's role in strength-ductility trade-off in polycrystalline Fe–Cr–Ni stainless steels produced by laser powder bed fusion, *Mater. Sci. Eng., A* 814 (March) (2021), <https://doi.org/10.1016/j.msea.2021.141214>.
- [25] T. Voisin, et al., New insights on cellular structures strengthening mechanisms and thermal stability of an austenitic stainless steel fabricated by laser powder-bed-fusion, *Acta Mater.* 203 (2021), <https://doi.org/10.1016/j.actamat.2020.11.018>.
- [26] L. Cui, et al., Superior low cycle fatigue property from cell structures in additively manufactured 316L stainless steel, *J. Mater. Sci. Technol.* 111 (2022) 268–278, <https://doi.org/10.1016/j.jmst.2021.10.006>.
- [27] E. Tascioglu, Y. Karabulut, Y. Kaynak, Influence of heat treatment temperature on the microstructural, mechanical, and wear behavior of 316L stainless steel fabricated by laser powder bed additive manufacturing, *Int. J. Adv. Manuf. Technol.* 107 (5–6) (2020) 1947–1956, <https://doi.org/10.1007/s00170-020-04972-0>. Mar.
- [28] Y. Chen, et al., Deformation mechanisms of selective laser melted 316L austenitic stainless steel in high temperature low cycle fatigue, *Mater. Sci. Eng., A* 843 (April) (2022) 143123, <https://doi.org/10.1016/j.msea.2022.143123>.
- [29] N. Haghdadi, M. Laleh, M. Moyle, S. Primig, Additive manufacturing of steels: a review of achievements and challenges, *J. Mater. Sci.* 56 (1) (2021) 64–107, <https://doi.org/10.1007/s10853-020-05109-0>.
- [30] G. Álvarez, Z. Harris, K. Wada, C. Rodríguez, E. Martínez-Pañeda, Hydrogen embrittlement susceptibility of additively manufactured 316L stainless steel: influence of post-processing, printing direction, temperature and pre-straining, *Addit. Manuf.* 78 (Sep) (2023), <https://doi.org/10.1016/j.addma.2023.103834>.
- [31] M. Pelegatti, D. Benasciutti, F. De Bona, A. Lanzutti, J.S. Novak, E. Salvati, Strain-controlled fatigue loading of an additively manufactured AISI 316L steel: cyclic plasticity model and strain-life curve with a comparison to the wrought material, *Fatig. Fract. Eng. Mater. Struct.* (February) (2023) 2195–2211, <https://doi.org/10.1111/ffe.13992>.
- [32] C.H. Yu, A. Leicht, R.L. Peng, J. Moverare, Low cycle fatigue of additively manufactured thin-walled stainless steel 316L, *Mater. Sci. Eng., A* 821 (2021), <https://doi.org/10.1016/j.msea.2021.141598>. Jul.
- [33] J. Man, et al., Formation of deformation induced martensite in fatigued 316L steels manufactured by selective laser melting (SLM), *Procedia Struct. Integr.* 43 (2022) 203–208, <https://doi.org/10.1016/j.prostr.2022.12.259>.
- [34] P. Kumar, R. Jayaraj, J. Suryawanshi, U.R. Satwik, J. McKinnell, U. Ramamurty, Fatigue strength of additively manufactured 316L austenitic stainless steel, *Acta Mater.* 199 (2020) 225–239, <https://doi.org/10.1016/j.actamat.2020.08.033>.
- [35] J.J. Lewandowski, M. Seifi, Metal additive manufacturing: a review of mechanical properties, *Annu. Rev. Mater. Res.* 46 (2016) 151–186, <https://doi.org/10.1146/annurev-matsci-070115-032024>.
- [36] P.D. Nezhadfar, K. Anderson-Wedge, S.R. Daniewicz, N. Phan, S. Shao, N. Shamsaei, Improved high cycle fatigue performance of additively manufactured 17-4 PH stainless steel via in-process refining micro-/defect-structure, *Addit. Manuf.* 36 (September) (2020) 101604, <https://doi.org/10.1016/j.addma.2020.101604>.
- [37] A. Yadollahi, N. Shamsaei, S.M. Thompson, A. Elwany, L. Bian, Effects of building orientation and heat treatment on fatigue behavior of selective laser melted 17-4 PH stainless steel, *Int. J. Fatig.* 94 (2017) 218–235, <https://doi.org/10.1016/j.ijfatigue.2016.03.014>.
- [38] M. Pelegatti, et al., On the factors influencing the elastoplastic cyclic response and low cycle fatigue failure of AISI 316L steel produced by laser-powder bed fusion, *Int. J. Fatig.* 165 (August) (2022) 107224, <https://doi.org/10.1016/j.ijfatigue.2022.107224>.
- [39] A. Averardi, C. Cola, S.E. Zeltmann, N. Gupta, Effect of particle size distribution on the packing of powder beds: a critical discussion relevant to additive manufacturing, *Mater. Today Commun.* 24 (9) (2020) 100964, <https://doi.org/10.1016/j.mtcomm.2020.100964>.
- [40] B.S. Rao, T.B. Rao, Effect of process parameters on powder bed fusion maraging steel 300: a review, *Lasers Manufacturing Mater. Processing* 9 (3) (2022) 338–375, <https://doi.org/10.1007/s40516-022-00182-6>.
- [41] L. Morichelli, E. Santecchia, M. Rossi, Combined effect of process variables on the plastic behaviour of 316L stainless steel printed by L-PBF, *Strain* 59 (March) (2023) 1–17, <https://doi.org/10.1111/str.12438>.
- [42] E. Salvati, A. Tognan, L. Laurenti, M. Pelegatti, F. De Bona, A defect-based physics-informed machine learning framework for fatigue finite life prediction in additive manufacturing, *Mater. Des.* 222 (2022) 111089, <https://doi.org/10.1016/j.matdes.2022.111089>.
- [43] N. Kazantseva, M. Il'nikh, V. Kuznetsov, Y. Koemets, K. Bakhrunov, M. Karabanalov, Design and structural factors' influence on the fatigue life of steel products with additive manufacturing, *Materials* 16 (23) (2023), <https://doi.org/10.3390/ma16237315>.
- [44] M. Benedetti, V. Fontanari, M. Bandini, F. Zanini, S. Carmignato, Low- and high-cycle fatigue resistance of Ti-6Al-4V ELI additively manufactured via selective laser melting: mean stress and defect sensitivity, *Int. J. Fatig.* 107 (November 2017) (2018) 96–109, <https://doi.org/10.1016/j.ijfatigue.2017.10.021>.
- [45] A. Avanzini, Fatigue behavior of additively manufactured stainless steel 316L, *Materials* 16 (1) (2023), <https://doi.org/10.3390/ma16010065>.
- [46] Q. Wang, et al., The cyclic deformation behavior and microstructural evolution of 304L steel manufactured by selective laser melting under various temperatures, *Mater. Sci. Eng., A* 891 (October 2023) (2024) 145949, <https://doi.org/10.1016/j.msea.2023.145949>.
- [47] T. Mei, Q. Wang, M. Liu, Y. Jiang, T. Zou, Y. Cai, The low-cycle fatigue behavior, microstructure evolution, and life prediction of SS 304: influence of temperature, *Materials* 16 (September) (2023) 1–19.
- [48] J. Gubicza, K. Mukhtarova, M. Kawasaki, Nanostructuring of additively manufactured 316L stainless steel using high-pressure torsion technique: an X-ray line profile analysis study, *Materials* 17 (45) (2024).
- [49] A. Lanzutti, M. Magnan, E. Vaglio, G. Totis, M. Sortino, L. Fedrizzi, Study of the effect of L-PBF technique temporal evolution on microstructure, surface texture, and fatigue performance of Ti gr. 23 alloy, *Metals* 13 (1247) (2023) 1–19, <https://doi.org/10.3390/met13071247>.
- [50] P. Bajaj, A. Hariharan, A. Kini, P. Kürmsteiner, D. Raabe, E.A. Jäggle, Steels in additive manufacturing: a review of their microstructure and properties, *Mater. Sci. Eng.* 772 (October 2019) (2020), <https://doi.org/10.1016/j.msea.2019.138633>.
- [51] T. Poulain, J. Mendez, G. Henaff, L. De Baglion, Characterization of damage during low cycle fatigue of a 304L austenitic stainless steel as a function of environment (air, PWR environment) and surface finish (polished, ground), *Procedia Eng.* 160 (September) (2016) 123–130, <https://doi.org/10.1016/j.proeng.2016.08.871>.
- [52] L. De Baglion, J. Mendez, Low cycle fatigue behavior of a type 304L austenitic stainless steel in air or in vacuum, at 20 °C or at 300 °C: relative effect of strain rate and environment, *Procedia Eng.* 2 (1) (2010) 2171–2179, <https://doi.org/10.1016/j.proeng.2010.03.233>.
- [53] M.S. Pham, S.R. Holdsworth, K.G.F. Janssens, E. Mazza, Cyclic deformation response of AISI 316L at room temperature: mechanical behaviour, microstructural evolution, physically-based evolutionary constitutive modelling, *Int. J. Plast.* 47 (2013) 143–164, <https://doi.org/10.1016/j.ijplas.2013.01.017>.
- [54] M.S. Pham, C. Solenthaler, K.G.F. Janssens, S.R. Holdsworth, Dislocation structure evolution and its effects on cyclic deformation response of AISI 316L stainless steel, *Mater. Sci. Eng., A* 528 (7–8) (2011) 3261–3269, <https://doi.org/10.1016/j.msea.2011.01.015>.
- [55] O. Muránsky, L. Balogh, M. Tran, C.J. Hamelin, J.S. Park, M.R. Daymond, On the measurement of dislocations and dislocation substructures using EBSD and HRSD

- techniques, *Acta Mater.* 175 (2019) 297–313, <https://doi.org/10.1016/j.actamat.2019.05.036>.
- [56] L. Liu, et al., Dislocation network in additive manufactured steel breaks strength–ductility trade-off, *Mater. Today* 21 (4) (2018) 354–361, <https://doi.org/10.1016/j.mattod.2017.11.004>.
- [57] P. Li, S.X. Li, Z.G. Wang, Z.F. Zhang, Unified factor controlling the dislocation evolution of fatigued face-centered cubic crystals, *Acta Mater.* 129 (2017) 98–111, <https://doi.org/10.1016/j.actamat.2017.02.057>.
- [58] P.E.J. Rivera-Díaz-Del-Castillo, M. Huang, Dislocation annihilation in plastic deformation: I. Multiscale irreversible thermodynamics, *Acta Mater.* 60 (6–7) (2012) 2606–2614, <https://doi.org/10.1016/j.actamat.2012.01.027>.
- [59] U. Führer, J. Aktaa, Modeling the cyclic softening and lifetime of ferritic-martensitic steels under creep-fatigue loading, *Int. J. Mech. Sci.* 136 (2018) 460–474, <https://doi.org/10.1016/j.ijmecsci.2017.12.042>.
- [60] T. Pereira, J. V. Kennedy, J. Potgieter, A comparison of traditional manufacturing vs additive manufacturing, the best method for the job, *Procedia Manuf.* 30 (2019) 11–18, <https://doi.org/10.1016/j.promfg.2019.02.003>.
- [61] K. Kellens, M. Baumanns, T.G. Gutowsky, W. Flanagan, R. Lifset, J.R. Duflou, Environmental dimensions of additive manufacturing: mapping application domains and their environmental implications, *J. Ind. Ecol.* 21 (1) (2017) 1–20, <https://doi.org/10.1111/jiec.12629>.
- [62] A. Sola, A. Nouri, Microstructural porosity in additive manufacturing: the formation and detection of pores in metal parts fabricated by powder bed fusion, *J. Adv. Manuf. Process* 1 (3) (2019), <https://doi.org/10.1002/amp2.10021>.
- [63] M. Ahmed Obeidi, et al., Comparison of the porosity and mechanical performance of 316L stainless steel manufactured on different laser powder bed fusion metal additive manufacturing machines, *J. Mater. Res. Technol.* 13 (2021) 2361–2374, <https://doi.org/10.1016/j.jmrt.2021.06.027>.
- [64] S. Tammam-Williams, P.J. Withers, I. Todd, P.B. Prangnell, The influence of porosity on fatigue crack initiation in additively manufactured titanium components, *Sci. Rep.* (June) (2017) 1–13, <https://doi.org/10.1038/s41598-017-06504-5>.
- [65] A.Y. Al-Maharma, S.P. Patil, B. Markert, Effects of porosity on the mechanical properties of additively manufactured components: a critical review, *Mater. Res. Express* (2020) 122001.
- [66] E.H. Valente, C. Gundlach, T.L. Christiansen, M.A.J. Somers, Effect of scanning strategy during selective laser melting on surface topography, porosity, and microstructure of additively manufactured Ti-6Al-4V, *Appl. Sci.* 9 (24) (2019), <https://doi.org/10.3390/app9245554>. Dec.
- [67] J.C. Fox, S.P. Moylan, B.M. Lane, Effect of process parameters on the surface roughness of overhanging structures in laser powder bed fusion additive manufacturing, *Procedia CIRP* 45 (2016) 131–134, <https://doi.org/10.1016/j.procir.2016.02.347>.
- [68] W. Beard, R. Lancaster, N. Barnard, T. Jones, J. Adams, The influence of surface finish and build orientation on the low cycle fatigue behaviour of laser powder bed fused stainless steel 316L, *Mater. Sci. Eng., A* 864 (December 2022) (2023) 144593, <https://doi.org/10.1016/j.msea.2023.144593>.
- [69] N. Bastola, M.P. Jahan, N. Rangasamy, A review of the residual stress generation in metal additive manufacturing : analysis of cause , measurement , effects , and prevention, *Micromachines* 14 (2023) 1–30.
- [70] Z. Fang, Z. Wu, C. Huang, C. Wu, Review on residual stress in selective laser melting additive manufacturing of alloy parts, *Opt Laser. Technol.* 129 (15) (2020) 106283, <https://doi.org/10.1016/j.optlastec.2020.106283>.
- [71] M.N. James, D.J. Hughes, Z. Chen, D.G. Hattings, P.J. Webster, S. Africa, Residual stresses and fatigue performance, *Eng. Fail. Anal.* 14 (2) (2007) 384–395.
- [72] T. Fritsch, et al., On the determination of residual stresses in additively manufactured lattice structures, *J. Appl. Crystallogr.* 54 (2021) 228–236, <https://doi.org/10.1107/S1600576720015344>.
- [73] D. Guo, et al., Solidification microstructure and residual stress correlations in direct energy deposited type 316L stainless steel, *Mater. Des.* 207 (2021) 109782, <https://doi.org/10.1016/j.matdes.2021.109782>.
- [74] Z. Fang, Z. Wu, C. Huang, C. Wu, Review on residual stress in selective laser melting additive manufacturing of alloy parts, *Opt Laser. Technol.* 129 (15) (2020) 106283, <https://doi.org/10.1016/j.optlastec.2020.106283>.
- [75] T. Poulain, J. Mendez, G. Henaff, L. De Baglion, Characterization of damage during low cycle fatigue of a 304L austenitic stainless steel as a function of environment (air, PWR environment) and surface finish (polished, ground), *Procedia Eng.* 160 (September) (2016) 123–130, <https://doi.org/10.1016/j.proeng.2016.08.871>.
- [76] F. Concli, R. Gerosa, D. Panzeri, L. Fraccaroli, High and low cycle fatigue properties of selective laser melted AISI 316L and AISI10Mg, *Int. J. Fatig.* 177 (July) (2023) 107931, <https://doi.org/10.1016/j.ijfatigue.2023.107931>.
- [77] T.M. Mower, M.J. Long, Mechanical behavior of additive manufactured, powder-bed laser-fused materials, *Mater. Sci. Eng., A* 651 (2016) 198–213, <https://doi.org/10.1016/j.msea.2015.10.068>.
- [78] D. Gonzalez-Nino, T. Strasser, G.S. Prinz, Ultra low-cycle fatigue behavior comparison between additively manufactured and rolled 17-4 ph (Aisi 630) stainless steels, *Metals* 11 (11) (2021), <https://doi.org/10.3390/met11111726>. Nov.
- [79] M. Laleh, et al., Heat treatment for metal additive manufacturing, *Prog. Mater. Sci.* 133 (July 2022) (2023) 101051, <https://doi.org/10.1016/j.pmatsci.2022.101051>.
- [80] E. Maleki, S. Bagherifard, M. Bandini, M. Guagliano, Surface post-treatments for metal additive manufacturing: progress, challenges, and opportunities, *Addit. Manuf.* 37 (1) (2020) 101619, <https://doi.org/10.1016/j.addma.2020.101619>.
- [81] E. Maleki, S. Bagherifard, A. Heydari Astaraee, S. Sgarbazzini, M. Bandini, M. Guagliano, Application of gradient severe shot peening as a novel mechanical surface treatment on fatigue behavior of additively manufactured AISI10Mg, *Mater. Sci. Eng., A* 881 (June) (2023) 145397, <https://doi.org/10.1016/j.msea.2023.145397>.
- [82] P.C. Priarone, A.R. Catalano, L. Settineri, Additive manufacturing for the automotive industry : on the life - cycle environmental implications of material substitution and lightweighting through re - design, *Progress Additive Manufacturing* (2023) 0123456789, <https://doi.org/10.1007/s40964-023-00395-x>.
- [83] L. Cui, et al., Superior low cycle fatigue property from cell structures in additively manufactured 316L stainless steel, *J. Mater. Sci. Technol.* 111 (2022) 268–278, <https://doi.org/10.1016/j.jmst.2021.10.006>.
- [84] L. Xu, S. Yang, L. Zhao, Y. Han, H. Jing, K. Wang, Low cycle fatigue behavior and microstructure evolution of a novel Fe-22Cr-15Ni austenitic heat-resistant steel, *J. Mater. Res. Technol.* 9 (6) (2020) 14388–14400, <https://doi.org/10.1016/j.jmrt.2020.09.121>.
- [85] S.S. Yadav, S.C. Roy, J. Veerababu, S. Goyal, Type-I to Type-II non-Masing behavior of 304L SS under low cycle fatigue: material's internal changes, *Int. J. Fatig.* 175 (2023) 107789, <https://doi.org/10.1016/j.ijfatigue.2023.107789>.
- [86] C. Bean, et al., Heterogeneous slip localization in an additively manufactured 316L stainless steel, *Int. J. Plast.* 159 (September) (2022) 103436, <https://doi.org/10.1016/j.ijplas.2022.103436>.
- [87] S. Bahl, S. Mishra, K.U. Yazar, I.R. Kola, K. Chatterjee, S. Suwas, Non-equilibrium microstructure, crystallographic texture and morphological texture synergistically result in unusual mechanical properties of 3D printed 316L stainless steel, *Addit. Manuf.* 28 (2019) 65–77, <https://doi.org/10.1016/j.addma.2019.04.016>.
- [88] X. Wang, J.A. Muñoz-Lerma, M. Attarian Shandiz, O. Sanchez-Mata, M. Brochu, Crystallographic-orientation-dependent tensile behaviours of stainless steel 316L fabricated by laser powder bed fusion, *Mater. Sci. Eng., A* 766 (June) (2019) 138395, <https://doi.org/10.1016/j.msea.2019.138395>.
- [89] P. Villechaise, M. Mineur, J. Mendez, Analysis of texture effects on fatigue behaviour of 316L stainless steel, *J. Phys. IV : JP* 11 (4) (2001), <https://doi.org/10.1051/jp4:2001438>.
- [90] T. Rautio, M. Jaskari, T. Gundigre, T. Iso-Junno, M. Vippola, A. Järvenpää, The effect of severe shot peening on fatigue life of laser powder bed fusion manufactured 316L stainless steel, *Materials* 15 (10) (2022) 1–13, <https://doi.org/10.3390/ma15103517>.
- [91] C.M. Smudde, C.R. D'Elia, C.W. San Marchi, M.R. Hill, J.C. Gibeling, The influence of residual stress on fatigue crack growth rates of additively manufactured type 304L stainless steel, *Int. J. Fatig.* 162 (April) (2022) 106954, <https://doi.org/10.1016/j.ijfatigue.2022.106954>.
- [92] W.J. Lai, A. Ojha, Z. Li, C. Engler-Pinto, X. Su, Effect of residual stress on fatigue strength of 316L stainless steel produced by laser powder bed fusion process, *Progress Additive Manufacturing* 6 (3) (2021) 375–383, <https://doi.org/10.1007/s40964-021-00164-8>.
- [93] H. Zhang, et al., Microstructure, surface quality, residual stress, fatigue behavior and damage mechanisms of selective laser melted 304L stainless steel considering building direction, *Addit. Manuf.* 46 (June) (2021) 102147, <https://doi.org/10.1016/j.addma.2021.102147>.
- [94] I. Serrano-Munoz, et al., On the interplay of microstructure and residual stress in LPBF IN718, *J. Mater. Sci.* 56 (9) (2021) 5845–5867, <https://doi.org/10.1007/s10853-020-05553-y>.
- [95] D.W. Brown, et al., Using in situ neutron diffraction to isolate specific features of additively manufactured microstructures in 304L stainless steel and identify their effects on macroscopic strength, *Metall. Mater. Trans. A Phys. Metall. Mater. Sci.* 50 (7) (2019) 3399–3413, <https://doi.org/10.1007/s11661-019-05240-x>.
- [96] A. Plotkowski, K. Saleeby, C.M. Fancher, J. Haley, G. Madiredy, S.S. Babu, Operando neutron diffraction reveals mechanisms for controlled strain evolution in 3D printing, *Nat. Commun.* 14 (8) (2023) 1–11, <https://doi.org/10.1038/s41467-023-40456-x>.
- [97] R.J. Williams, F. Vecchiato, J. Kelleher, M.R. Wenman, P.A. Hooper, C.M. Davies, Effects of heat treatment on residual stresses in the laser powder bed fusion of 316L stainless steel: finite element predictions and neutron diffraction measurements, *J. Manuf. Process.* 57 (2020) 641–653, <https://doi.org/10.1016/j.jmapro.2020.07.023>. December 2019.
- [98] J. Schröder, et al., Texture-based residual stress analysis of laser powder bed fused Inconel 718 parts, *J. Appl. Crystallogr.* 56 (4) (2023) 1–15, <https://doi.org/10.1107/S1600576723004855>.
- [99] J. Schröder, et al., Diffraction-based residual stress characterization in laser additive manufacturing of metals 11 (11) (2021), <https://doi.org/10.3390/met11111830>.
- [100] X. Cheng, H. J. T. Gnaeupel-Herold, V. Luzin, W. J. Neutron diffraction measurements for residual stresses in Al-6XN stainless steel welded beams, *Neutron Diffraction* (2012), <https://doi.org/10.5772/37537>. March.
- [101] A. Charmi, et al., Mechanical anisotropy of additively manufactured stainless steel 316L : an experimental and numerical study, *Mater. Sci. Eng., A* 799 (June 2020) (2021) 140154, <https://doi.org/10.1016/j.msea.2020.140154>.
- [102] A. Ulbricht, et al., Separation of the formation mechanisms of residual stresses in lpbf 316L : an experimental and numerical study, *Mater. Sci. Eng., A* 799 (June 2020) (2021) 140154, <https://doi.org/10.1016/j.msea.2020.140154>.
- [103] S. Goel, et al., Residual stress determination by neutron diffraction in powder bed fusion-built Alloy 718: influence of process parameters and post-treatment, *Mater. Des.* 195 (2020) 109045, <https://doi.org/10.1016/j.matdes.2020.109045>.

- [104] S. Tang, V. Luzin, C. Yang, W. Zhang, Z. Wang, Revealing the macroscale texture in an additive manufactured Co-Cr-Mo alloy by neutron diffraction, *Mater. Char.* 205 (April) (2023) 113243, <https://doi.org/10.1016/j.matchar.2023.113243>.
- [105] D.W. Brown, et al., In-situ neutron diffraction study of the influence of microstructure on the mechanical response of additively manufactured 304L stainless steel, *Metall. Mater. Trans. A Phys. Metall. Mater. Sci.* 48 (2017) 6055–6069, <https://doi.org/10.1007/s11661-017-4330-4>.
- [106] A. Brule, O. Kirstein, Residual stress diffractometer KOWARI at the Australian research reactor OPAL: status of the project, *Phys. B Condens. Matter* 385–386 (2006) 1040–1042, <https://doi.org/10.1016/j.physb.2006.05.333>.
- [107] J. Schröder, et al., Diffraction-based residual stress characterization in laser additive manufacturing of metals 11 (11) (2021), <https://doi.org/10.3390/met11111830>.
- [108] H. Choo, M.R. Koehler, L.P. White, Y. Ren, D. Morin, E. Garlea, *Materials Science & Engineering A Influence of defect characteristics on tensile deformation of an additively manufactured stainless steel : evolutions of texture and intergranular strain*, *Mater. Sci. Eng., A* 791 (February) (2020) 139637, <https://doi.org/10.1016/j.msea.2020.139637>.
- [109] R.A. Winholtz, *Characterization of macrostresses*, in: M.E. Fitzpatrick, A. Lodini (Eds.), *Analysis of Residual Stress by Diffraction Using Neutron and Synchrotron Radiation*, first ed., Taylor & Francis, 2003.
- [110] F. Bachmann, R. Hielscher, H. Schaeben, Texture analysis with MTEX- Free and open source software toolbox, *Solid State Phenom.* 160 (2010) 63–68, <https://doi.org/10.4028/www.scientific.net/SSP.160.63>.
- [111] F. Bachmann, R. Hielscher, H. Schaeben, Grain detection from 2d and 3d EBSD data-Specification of the MTEX algorithm, *Ultramicroscopy* 111 (12) (2011) 1720–1733, <https://doi.org/10.1016/j.ultramic.2011.08.002>.
- [112] R. Hielscher, H. Schaeben, A novel pole figure inversion method: specification of the MTEX algorithm, *J. Appl. Crystallogr.* 41 (6) (2008) 1024–1037, <https://doi.org/10.1107/S0021889808030112>.
- [113] U. Welzel, E.J. Mittemeijer, Diffraction stress analysis of macroscopically elastically anisotropic specimens : on the concepts of diffraction elastic constants and stress factors, *J. Appl. Phys.* 9001 (2003) (2012), <https://doi.org/10.1063/1.1569662>.
- [114] D. Mainprice, F. Bachmann, R. Hielscher, H. Schaeben, Descriptive tools for the analysis of texture projects with large datasets using MTEX: strength, symmetry and components, *Geol. Soc. Spec. Publ.* 409 (1) (2015) 251–271, <https://doi.org/10.1144/SP409.8>.
- [115] M. Avdeev, J.R. Hester, ECHIDNA : a Decade of High-Resolution Neutron Powder Diffraction at OPAL Research Papers, 2018, pp. 1597–1604, <https://doi.org/10.1107/S1600576718014048>.
- [116] P. Scardi, M. Leoni, Whole powder pattern modelling, *Acta Crystallogr. A Found Adv.* 58 (2002) 190–200.
- [117] M. Leoni, “International tables for crystallography, in: *International Tables for Crystallography*, 2019, pp. 289–298, 2019.
- [118] M. Leoni, T. Confente, P. Scardi, PM2K: a flexible program implementing whole powder pattern modelling, *Z. Kristallographie, Supplement 1* (23) (2006) 249–254, <https://doi.org/10.1524/zksu.2006.suppl.23.249>.
- [119] N. Armstrong, M. Leoni, P. Scardi, Considerations concerning Wilkens’ theory of dislocation line-broadening, *Z. Kristallographie, Supplement 1* (23) (2006) 81–86, <https://doi.org/10.1524/zksu.2006.suppl.23.81>.
- [120] T. Ungár, Dislocation model of strain anisotropy, *Powder Diffr.* 23 (2) (2008) 125–132, <https://doi.org/10.1154/1.2918549>.
- [121] J. Martínez-García, M. Leoni, P. Scardi, A general approach for determining the diffraction contrast factor of straight-line dislocations, *Acta Crystallogr. A* 65 (2) (2009) 109–119, <https://doi.org/10.1107/S010876730804186X>.
- [122] R. Douglas, et al., The influence of energy density on the low cycle fatigue behaviour of laser powder bed fused stainless steel 316L, *Int. J. Fatig.* (2023) 108123, <https://doi.org/10.1016/j.ijfatigue.2023.108123>. Apr.
- [123] F. Bachmann, R. Hielscher, H. Schaeben, Texture analysis with MTEX- Free and open source software toolbox, *Solid State Phenom.* 160 (2010) 63–68, <https://doi.org/10.4028/www.scientific.net/SSP.160.63>.
- [124] A. Janda, S. Ebenbauer, A. Prestil, I. Siller, H. Clemens, P. Spoerk-Erdely, In-situ high-temperature EBSD characterization during a solution heat treatment of hot-rolled Ti-6Al-4V, *Mater. Char.* 192 (August) (2022) 112207, <https://doi.org/10.1016/j.matchar.2022.112207>.
- [125] A.J. Wilkinson, T. Ben Britton, Strains, planes, and EBSD in materials science, *Mater. Today* 15 (9) (2012) 366–376, [https://doi.org/10.1016/S1369-7021\(12\)70163-3](https://doi.org/10.1016/S1369-7021(12)70163-3).
- [126] F. Bachmann, R. Hielscher, H. Schaeben, Grain detection from 2d and 3d EBSD data-Specification of the MTEX algorithm, *Ultramicroscopy* 111 (12) (2011) 1720–1733, <https://doi.org/10.1016/j.ultramic.2011.08.002>.
- [127] R. Ullah, J. Lu, L. Sang, M. Rizwan, Y. Zhang, Z. Zhang, Investigating the microstructural evolution during deformation of laser additive manufactured Ti – 6Al – 4V at 400 °C using in-situ EBSD, *Mater. Sci. Eng., A* 823 (July) (2021) 141761, <https://doi.org/10.1016/j.msea.2021.141761>.
- [128] S.I. Wright, J. Kacher, T. Ruggles, *Electron Backscatter Diffraction Based Strain Analysis in the Scanning Electron Microscope*, 2021, pp. 1–31.
- [129] M.J. McLean, W.A. Osborn, In-situ elastic strain mapping during micromechanical testing using EBSD, *Ultramicroscopy* 185 (2018) 21–26, <https://doi.org/10.1016/j.ultramic.2017.11.007>. Feb.
- [130] F.C. Pinto, L.S. Aota, I.R. Souza Filho, D. Raabe, H.R.Z. Sandim, Recrystallization in non-conventional microstructures of 316L stainless steel produced via laser powder-bed fusion: effect of particle coarsening kinetics, *J. Mater. Sci.* 57 (21) (2022) 9576–9598, <https://doi.org/10.1007/s10853-021-06859-1>.
- [131] Z. Hu, et al., Micro laser powder bed fusion of stainless steel 316L: cellular structure, grain characteristics, and mechanical properties, *Mater. Sci. Eng., A* 848 (April) (2022) 143345, <https://doi.org/10.1016/j.msea.2022.143345>.
- [132] D. Kumar Pandey, P. Kumar Verma, A. Bhattacharyya, A. Sarkar, A Back-stress deconvolution method towards modelling of low cycle fatigue behavior of type 316L(N) stainless steel at room temperature, *Int. J. Fatig.* 166 (April 2022) (2023), <https://doi.org/10.1016/j.ijfatigue.2022.107297>.
- [133] J. Zhou, Z. Sun, P. Kanouté, D. Retraint, Experimental analysis and constitutive modelling of cyclic behaviour of 316L steels including hardening/softening and strain range memory effect in LCF regime, *Int. J. Plast.* 107 (2018) 54–78, <https://doi.org/10.1016/j.ijplas.2018.03.013>.
- [134] C.-H. Yu, et al., Effect of stress relief heat treatment on low cycle fatigue behaviours of LPBF stainless steel 316L, <https://doi.org/10.2139/ssrn.4159502>, 2022.
- [135] J. Liu, et al., Dislocation strengthening without ductility trade-off in metastable austenitic steels, *Sci. Rep.* 6 (September) (2016) 1–10, <https://doi.org/10.1038/srep35345>.
- [136] C. Zhu, T. Harrington, G.T. Gray, K.S. Vecchio, Dislocation-type evolution in quasi-statically compressed polycrystalline nickel, *Acta Mater.* 155 (May) (2018) 104–116, <https://doi.org/10.1016/j.actamat.2018.05.022>.
- [137] E. Schafner, M. Zehetbauer, T. Ungár, Measurement of screw and edge dislocation density by means of X-ray Bragg profile analysis, *Mater. Sci. Eng., A* 319–321 (2001) 220–223, [https://doi.org/10.1016/S0921-5093\(01\)00979-0](https://doi.org/10.1016/S0921-5093(01)00979-0).
- [138] G. Bergeret, P. Gallezot, G. Bergeret, P. Gallezot, P. Size, D. Measurements, Particle size and dispersion measurements, in: *Handbook of Heterogeneous Catalysis*, second ed., Wiley-VCH, 2008, pp. 738–765.
- [139] D.D.R. Peachey, et al., Directional recrystallization of an additively manufactured Ni-base superalloy, *Addit. Manuf.* 60 (PA) (2022) 103198, <https://doi.org/10.1016/j.addma.2022.103198>.
- [140] M.F. Ashby, The deformation of plastically non-homogeneous materials, *Phil. Mag.* 21 (170) (1969) 37–41.
- [141] T. Voisin, et al., New insights on cellular structures strengthening mechanisms and thermal stability of an austenitic stainless steel fabricated by laser powder-bed-fusion, *Acta Mater.* 203 (2021), <https://doi.org/10.1016/j.actamat.2020.11.018>.
- [142] M.S. Pham, B. Dovgvy, P.A. Hooper, C.M. Gourlay, A. Pignone, The role of side-branching in microstructure development in laser powder-bed fusion, *Nat. Commun.* 11 (1) (2020) 1–12, <https://doi.org/10.1038/s41467-020-14453-3>.
- [143] F. Wang, et al., Dislocation cells in additively manufactured metallic alloys characterized by electron backscatter diffraction pattern sharpness, *Mater. Char.* 197 (January) (2023) 112673, <https://doi.org/10.1016/j.matchar.2023.112673>.
- [144] Y.M. Wang, et al., Additively manufactured hierarchical stainless steels with high strength and ductility, *Nat. Mater.* 17 (October) (2017) 63–71, <https://doi.org/10.1038/NMAT5021>.
- [145] E.W. Horton, et al., The inclusion and role of micro mechanical residual stress on deformation of stainless steel type 316L at grain level, *Mater. Sci. Eng., A* 876 (February) (2023) 145096, <https://doi.org/10.1016/j.msea.2023.145096>.
- [146] O. Voehringer, Relaxation of residual stresses by annealing or mechanical treatment, *Adv. Sur. Treat. Technol. - Appl. - Eff.* 4 (January 1987) (1987) 367–396, <https://doi.org/10.1016/b978-0-08-034062-3.50027-6>.
- [147] J. Zhao, Y. Hu, Q. Kan, H. Miao, G. Kang, Influence of build direction on the ratcheting-fatigue interaction of heat-treated additively manufactured 316L stainless steel, *Int. J. Fatig.* 181 (October 2023) (2024) 108143, <https://doi.org/10.1016/j.ijfatigue.2024.108143>.
- [148] M. Kamaya, A procedure for estimating Young’s modulus of textured polycrystalline materials, *Int. J. Solid Struct.* 46 (13) (2009) 2642–2649, <https://doi.org/10.1016/j.ijsolstr.2009.02.013>.